PNNL-24745

Pacific Northwest
NATIONAL LABORATORY

Proudly Operated by **Battelle** *Since 1965*

Improving Distribution Resiliency with Microgrids and State and Parameter Estimation

September 2015

FK Tuffner
TL Williams
KP Schneider
MA Elizondo
Y Sun
CC Liu
Y Xu
SN Gourisetti

U.S. DEPARTMENT OF
ENERGY

Prepared for the U.S. Department of Energy
under Contract DE-AC05-76RL01830

DISCLAIMER

This report was prepared as an account of work sponsored by an agency of the United States Government. Neither the United States Government nor any agency thereof, nor Battelle Memorial Institute, nor any of their employees, makes **any warranty, express or implied, or assumes any legal liability or responsibility for the accuracy, completeness, or usefulness of any information, apparatus, product, or process disclosed, or represents that its use would not infringe privately owned rights**. Reference herein to any specific commercial product, process, or service by trade name, trademark, manufacturer, or otherwise does not necessarily constitute or imply its endorsement, recommendation, or favoring by the United States Government or any agency thereof, or Battelle Memorial Institute. The views and opinions of authors expressed herein do not necessarily state or reflect those of the United States Government or any agency thereof.

PACIFIC NORTHWEST NATIONAL LABORATORY
operated by
BATTELLE
for the
UNITED STATES DEPARTMENT OF ENERGY
under Contract DE-AC05-76RL01830

Printed in the United States of America

Available to DOE and DOE contractors from the
Office of Scientific and Technical Information,
P.O. Box 62, Oak Ridge, TN 37831-0062;
ph: (865) 576-8401
fax: (865) 576-5728
email: reports@adonis.osti.gov

Available to the public from the National Technical Information Service
5301 Shawnee Rd., Alexandria, VA 22312
ph: (800) 553-NTIS (6847)
email: orders@ntis.gov <http://www.ntis.gov/about/form.aspx>
Online ordering: http://www.ntis.gov

♻ This document was printed on recycled paper.

(8/2010)

PNNL-24745

Improving Distribution Resiliency with Microgrids and State and Parameter Estimation

FK Tuffner
TL Williams
KP Schneider
MA Elizondo
Y Sun
CC Liu
Y Xu
SN Gourisetti

September 2015

Prepared for
the U.S. Department of Energy
under Contract DE-AC05-76RL01830

Pacific Northwest National Laboratory
Richland, Washington 99352

Abstract

Modern society relies on low-cost reliable electrical power, both to maintain industry, as well as provide basic social services to the populace. When major disturbances occur, such as Hurricane Katrina or Hurricane Sandy, the nation's electrical infrastructure can experience significant outages. To help prevent the spread of these outages, as well as facilitating faster restoration after an outage, various aspects of improving the resiliency of the power system are needed. Two such approaches are breaking the system into smaller microgrid sections, and to have improved insight into the operations to detect failures or mis-operations before they become critical.

Breaking the system into smaller sections of microgrid islands, power can be maintained in smaller areas where distribution generation and energy storage resources are still available, but bulk power generation is no longer connected. Additionally, microgrid systems can maintain service to local pockets of customers when there has been extensive damage to the local distribution system. However, microgrids are grid connected a majority of the time and implementing and operating a microgrid is much different than when islanded. This report discusses work conducted by the Pacific Northwest National Laboratory that developed improvements for simulation tools to capture the characteristics of microgrids and how they can be used to develop new operational strategies. These operational strategies reduce the cost of microgrid operation and increase the reliability and resilience of the nation's electricity infrastructure.

In addition to the ability to break the system into microgrids, improved observability into the state of the distribution grid can make the power system more resilient. State estimation on the transmission system already provides great insight into grid operations and detecting abnormal conditions by leveraging existing measurements. These transmission-level approaches are expanded to using advanced metering infrastructure and other distribution-level measurements to create a three-phase, unbalanced distribution state estimation approach. With distribution-level state estimation, the grid can be operated more efficiently, and outages or equipment failures can be caught faster, improving the overall resilience and reliability of the grid.

Acknowledgments

The authors wish to thank Mr. Dan Ton, with the United States Department of Energy, Office of Electricity Delivery and Energy Reliability (DOE-OE), for providing funding and guidance for this work. The authors also wish to thank Terry Ryan and David Kimbrel with the Washington State University (WSU) facilities department for their valuable help and insight into the WSU microgrid, as well as Heather Rosentrater and David James with Avista Utilities for their insights into the Pullman, Washington system. Finally, the authors wish to thank Jason Fuller at the Pacific Northwest National Laboratory, for providing the review and feedback on this document.

Acronyms and Abbreviations

AMI	Advanced Metering Infrastructure
CERTS	Consortium for Electric Reliability Technology Solutions
DMS	Distribution Management System
DOE	Department of Energy
DOE-OE	Department of Energy, Office of Electricity Delivery and Energy Reliability
DSSE	Distribution System State Estimation
EMS	Energy Management System
KF	Kalman Filter
MDM	Meter Data Management
PE	Parameter Estimation
PNNL	Pacific Northwest National Laboratory
SCADA	Supervisory Control and Data Acquisition
SE	State Estimation
WLS	Weighted Least Squares
WSU	Washington State University

Contents

Abstract iii
Acknowledgments v
Acronyms and Abbreviations vii
1.0 Introduction 1
  1.1 Traditional Mitigation 1
  1.2 Distribution Resiliency 1
2.0 Microgrids as a Resiliency Resource 3
  2.1 Previous Work 3
  2.2 Asset Feasibility 3
    2.2.1 Dynamic considerations 4
    2.2.2 Distribution line and transformer in-rush 7
    2.2.3 Resilience-Oriented Service Restoration and Reconfiguration 11
    2.2.4 Nomograms 19
  2.3 Consolidated approach 22
3.0 Distribution-level State Estimation and Parameter Estimation 25
  3.1 Background and Introduction 25
  3.2 Data and Measurements in Distribution Systems 28
  3.3 Distribution System State Estimation 29
    3.3.1 Weighted Least Squares Formulation for Distribution System State Estimation 29
    3.3.2 Simulation Studies 34
    3.3.3 Case 6: IEEE 8500 Node Test System 38
  3.4 Distribution System Parameter Estimation 39
    3.4.1 Methods 40
    3.4.2 Simulation Studies 42
  3.5 Conclusions and Future Work 47
4.0 Conclusions 48

Figures

Figure 1. Norton equivalent circuit representation of generator 6
Figure 2. Three-phase voltages for sample microgrid after load-shed event 6
Figure 3. Mechanical speed for generator in sample microgrid after load-shed event 7
Figure 4. Simple line in-rush example 9
Figure 5. Sample saturation curve for transformer showing flux-to-current relationship........ 9
Figure 6. Primary currents for saturated transformer during in-rush scenario 11
Figure 7. Post-event structure of a distribution system 12
Figure 8. One-line diagram of a 4-feeder 1069-bus test system 15
Figure 9. A simplified microgrid model 15
Figure 10. Transient frequency of (a) microgrid 1 and (b) microgrid 3........ 18
Figure 11. Critical load restoration strategy for Pullman-WSU system 19
Figure 12. Curves of (a) system frequency and (b) generator voltages 19
Figure 13. Notional diagram of Pullman system for simulation 20
Figure 14. Frequency response for two generators to various step load changes 21
Figure 15. Sample nomogram for frequency deviations of different generator combinations 21
Figure 16. Example reactive power nomogram for different transmission line lengths, voltage levels, and generator capabilities 23
Figure 17. Flow chart of evaluation methodology. 27
Figure 18. Principle components of a typical residential service system........ 29
Figure 19. Three-wire ungrounded delta line segment in single-phase approximation. 30
Figure 20. Four-wire grounded wye line segment. 32
Figure 21. Modified IEEE 13 Node Test System. 35
Figure 22. Plot of $|V_{err}|$ vs. AMI sample time........ 36
Figure 23. Plot of $|V_{err}|$ vs. number of AMI meters per secondary transformer. 37
Figure 24. Plot of $|V_{err}|$ as the unmetered load on phase *b* is increased........ 38
Figure 25. IEEE 8500 Node Test System. Fig reproduced from [58]........ 39
Figure 26. Estimated parameter error with no measurement noise and single snapshot using RA (in grey) and KF (in black) 44
Figure 27. Estimated parameter error with 1% measurement noise and single snapshot using RA (in grey) and KF (in black) 44
Figure 28. Estimated parameter error with 1% measurement noise and 12 combined time steps using RA (in grey) and KF approach (in black)........ 46

Tables

Table 1. Generation Capacity and Load Data for Microgrids 15
Table 2. Restoration Trees 16
Table 3. Load Groups 16
Table 4. 13 Node Test System $|V_{err}|$ Values in Percent 36
Table 5. 13 Node Test System $|V_{err}|$ Values with Limited SCADA Measurements 38
Table 6. Mean of PE errors using RA and KF 45
Table 7. Standard deviation of PE errors using RA and KF 45

1.0 Introduction

The nation's electrical infrastructure was originally developed as a collection of small isolated systems, such as Thomas Edison's Pearl Street Station in lower Manhattan. Over time, these systems were interconnected to increase reliability and reduce costs, leading to the electrical infrastructure that the nation has come to rely on. In recent years, an increase in the number and scale of blackouts, combined with advances in technology, has led to a re-examination of the basic premise of large interconnected power systems, especially during extreme weather events.

Work conducted over the past decade by national laboratories, universities, and industry has shown that segmenting portions of the distribution system during extreme events has the ability to provide uninterrupted service to critical end-use loads. Operating a portion of the distribution system as a microgrid has the technical potential to increase reliability and resilience, but it is an expensive solution to deploy and operate. As a result, it is necessary to develop tools and capabilities to reduce the design and operating costs of microgrids, as well as to develop new operating strategies that will increase the benefits that can be obtained from a microgrid once it has been deployed.

1.1 Traditional Mitigation

Traditional mitigation and prevention of power outages as a result of large-scale events can fall into two general, simple categories: infrastructure updates beforehand and isolated operations during the event. Infrastructure improvements are upgrades to the equipment and capabilities of the distribution system to prevent the anticipated effects a large scale event may cause. For example, equipment hardening is physically reinforcing or selecting equipment to prevent damage by common environmental factors. Examples include enclosures that are higher than expected flooding levels, or the utilization of water-proof connectors for all cable entrances and connections. The overall approach for infrastructure improvements is to either prevent the introduction of elements that would disable the equipment for long periods of time, or have backup and/or redundant capabilities to still supply that functionality.

Isolated operations during the event typically refer to traditional, on-site backup generation for facilities. When a large-scale power outage occurs, the on-site backup generator will provide power to a single facility or building. The reliability and resiliency of that load is increased, but little value is provided to nearby assets and no redundancy is in place for the local asset. While this provides great initial reliability and a small degree of resilience, the system is still subject to single-point failures, and the benefit only applies to a small footprint of operation.

1.2 Distribution Resiliency

Improving overall distribution resiliency can take many forms. The research represented in this report focuses on two approaches: using microgrids as a resiliency resource and implementing distribution-level state estimation. These two techniques can be deployed as a joint resource, or through separate installs, to improve the overall resiliency of the grid through continuity of operations.

Microgrids as a resiliency resource investigates the aspects of operating an islanded microgrid composed of switchgear, critical loads, and distributed generation. Utilizing the existing and surviving distribution power infrastructure, a single backup generator can provide load to a community resource, such as a nearby hospital or disaster relief center. Under the right circumstances, the distributed generation sources may even be useful to help with black start operations of a nearby power plant. Chapter 2 investigates the simulation capabilities and evaluation criteria for operating a microgrid as a local resource, a community resource, and as a black start resource.

Distribution-level state estimation improves resiliency through greater understanding of current system conditions. Even with the varying forms of telemetry now available on the distribution level, not every device is measured directly. Furthermore, degradation in transformers and cables may not be readily apparent in single measurement values, but become apparent in a time-series evaluation of measurements. Distribution-level state estimation leverages the existing distribution-level telemetry, such as that from advanced metering infrastructure (AMI), to detect states of devices on the system and provide a means to tracking equipment degradation. Such insights can lead to more efficient operation, as well as pre-emptive repairs, increasing the overall reliability and resiliency of the distribution system. Aspects and implementation considerations of distribution-level state estimation are discussed in Chapter 3.

While not explored in this report, the combination of the use of microgrids and distribution-level state estimation can provide even greater benefit to the overall resiliency of the system. Prior to the event, the distribution state-estimation can help detect equipment failures early, including those that form key components of the microgrids during the event. Once the event has occurred and the system is operating as microgrid islands, the distribution state estimation can continue to provide further insights into the system behavior. Some equipment failures on the microgrid can be detected early, and repaired or mitigated to prevent the failure of the full microgrid. Distribution state estimation can also provide indirect observability into devices that may have lost communication, such as switchgear or distributed generation. The state estimation can help determine if a switch is open or closed, or if some additional source of generation or load is present on the system that is not anticipated. This information can feed directly into the reconfiguration algorithms and operational considerations of the microgrid to help determine if further load could be restored, or if there is any additional capability for use in black start operations.

2.0 Microgrids as a Resiliency Resource

During a natural disaster or other power-interrupting event, existing generation and energy supply resources within a service territory can often be leveraged to restore basic public services faster, as well as aid in the overall restoration process. However, utilizing these existing assets is rarely as simple as just activating them. Dynamics of the system, electrical constraints of the equipment, and conditions of the disaster itself create a completely different set of operational conditions that need to be addressed. Over the past three years, the DOE-OE resiliency work has examined many of these issues, and provided a means to simulate, test, and mitigate different microgrids as resiliency resources.

2.1 Previous Work

The general concept of microgrids is not a new one, with standard backup generation serving the simplest form of this implementation. The DOE Consortium for Electric Reliability Technology Solutions (CERTS) work has examined many of the base microgrid control and feasibility considerations. The body of that research can be found at [1]. In addition to the CERTS-based research, there have been numerous academic studies into microgrids and microgrid controllers [2], [3]. However, much of this work has considered a green-field microgrid deployment, or deployment under ideal circumstances. In a larger, natural disaster scenario, existing assets that were never part of a larger microgrid may need to be leveraged. This can include equipment and areas that were not traditionally part of a microgrid or do not have a dedicated microgrid controller to coordinate their operation.

The DOE-OE-funded Microgrids as a Resiliency Resource research addresses many of these concerns. By improving the simulation tools, providing operational constraints for existing assets, and providing software-based restoration schemes, existing distribution systems could be leveraged to restore power faster after an outage, or keep certain critical loads maintained while the larger transmission grid is restored.

2.2 Asset Feasibility

Utilizing microgrids as a resiliency resource has many considerations. While equipment availability and connectivity to the power system are obviously two of the largest issues for utilizing microgrid assets, many more operational considerations must be considered. Distribution systems are often composed of many single-phase loads and laterals. This can result in an imbalance of the amount of power flowing on each of the three phases. Some generators have protective devices that can remove the generator when the imbalance is too great, in order to protect the generator equipment. Accurately modeling single-phase loads and laterals in the topology must be considered to ensure the generators are capable of safely supporting the system. Furthermore, the distributed generation resources available to a microgrid do not have the power producing and inertial capacity of the transmission power connection. This requires a more careful consideration for concerns such as in-rush and frequency deviations that the larger capacity transmission grid connection did not experience.

To assist in addressing these operational considerations and provide useful operational guidance, the DOE-OE-funded GridLAB-D [4] distribution-level simulator is utilized. The next sections describe some of the specific implementations in the GridLAB-D simulations used to capture new microgrid considerations. The sections culminate in the generation of operational nomograms, which can be used offline by emergency personnel to determine how to restore power to critical assets in the distribution network. The nomograms can also be used to evaluate potential actions on the microgrid and prevent an operation that may overload the system, helping maintain the power to critical assets already being utilized.

2.2.1 Dynamic considerations

A key consideration for the utilization of microgrids as a resiliency resource is the associated dynamic operations of the microgrid. With a much smaller generation source, and the characteristics of distribution systems, dynamics play a significantly larger role than they would during normal transmission-grid-connected operations. Along with reduced capabilities of the generation sources, the unbalanced nature of the distribution grid imposes some additional considerations.

During the first two years of the Microgrids as a Resiliency Resource program, the capability to simulate electromechanical machine dynamics and factor in unbalanced distribution considerations were added to the GridLAB-D platform. Details are available in previous reports and a journal publication [5]–[7]. Many existing GridLAB-D reports and papers outline the three-phase current injection method as the basis for all powerflow solutions, with those details readily available in [8]. While programs such as PSCAD can model the unbalanced distribution system, it provides results at the electromagnetic level, which is often useful for protection design, but not typically needed for operational considerations. Furthermore, this detail level makes implementing full distribution feeder models in PSCAD incredibly time-consuming, if not impossible. GridLAB-D was designed to model the full distribution system topology. Applying electromechanical simulation capabilities to this existing capability allows larger models to be explored, particularly when a microgrid is used to power a larger area of end-uses.

The basis for capturing the unbalanced electromechanical transients is interfacing with the powerflow solver, but also respecting the symmetrical constraints of the generator itself. The implementation begins with a standard set of machine equations for the stator voltages, simplified into the subset that follows. These equations are decomposed into direct, quadrature, and zero axis representations given by [9], which are a common representation for rotating electrical machines, the *dq0* model:

$$\frac{dE_d''}{dt} = \frac{\omega}{\omega_s} E_q'' + R_a I_q + V_q \tag{1}$$

$$\frac{dE_q''}{dt} = \frac{\omega}{\omega_s} E_d'' + R_a I_d + V_d \tag{2}$$

$$\frac{dE_0''}{dt} = R_0 I_0 + V_0 \tag{3}$$

where:

E_d'', E_q'', E_0''	Subtransient voltages for direct, quadrature, and zero axis,
I_d, I_q, I_0	Currents for direct, quadrature, and zero axis,
V_d, V_q, V_0	Machine terminal voltages for direct, quadrature, and zero axis,
R_a	Machine armature resistance,
R_0	Machine zero-sequence resistance,
ω	Machine rotor mechanical speed, and
ω_s	Machine rotor rated mechanical speed.

These equations represent the differential equations driving the machine dynamics and contain the constraints associated with the symmetrical build of a three-phase generator. To interface with the distribution-level dynamic system, this sequential component model must be translated to the three-phase unbalanced powerflow interface point. This is done by changing the machine interface into a Norton equivalent circuit [10]. A Norton-equivalent circuit models the device or system as a dependent current source, with a parallel impedance, as shown in Figure 1. The values in Figure 1 are calculated using the equations:

$$\mathbf{Y_{Ga,b,c}} = \mathbf{T_S} \begin{bmatrix} Y_{G0} & 0 & 0 \\ 0 & Y_{G1} & 0 \\ 0 & 0 & Y_{G2} \end{bmatrix} \mathbf{T_S^{-1}} \tag{4}$$

$$\mathbf{I_{GSa,b,c}} = \frac{1}{3} \begin{bmatrix} 1 \\ e^{\frac{j4\pi}{3}} \\ e^{\frac{j2\pi}{3}} \end{bmatrix} I_{GS1} \tag{5}$$

where:

Y_{G0}, Y_{G1}, Y_{G2}	Zero, positive, and negative sequence admittance for machine,
$\mathbf{T_S}$	Matrix to convert sequence terms to three-phase representation, and
I_{GS1}	Machine output current.

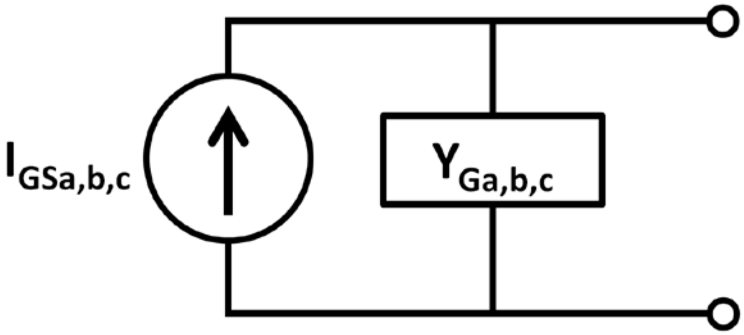

Figure 1. Norton equivalent circuit representation of generator

Utilizing equations (1) to (5) and the details further outlined in [7], the basis for the dynamics of microgrid or islanded systems can be properly represented. Figure 2 shows the voltage results for the IEEE 13-node system with two distributed, synchronous diesel reciprocating engine generators. The 13-node system is operating as an islanded microgrid and experiences a load shed event at 1.0 seconds of 485 kVA, or approximately 13% of the system load. As Figure 2 shows, the voltages are clearly unbalanced prior to the event, and even more so after the load shed. The colored sections of the figure represent validation results from PSCAD. Notice the higher frequency transients captured, which represent electromagnetic details of the model. While these are useful for explicit protection studies and harmonic analysis, many feasibility constraints for operating a microgrid as a resiliency resource do not require this level of detail.

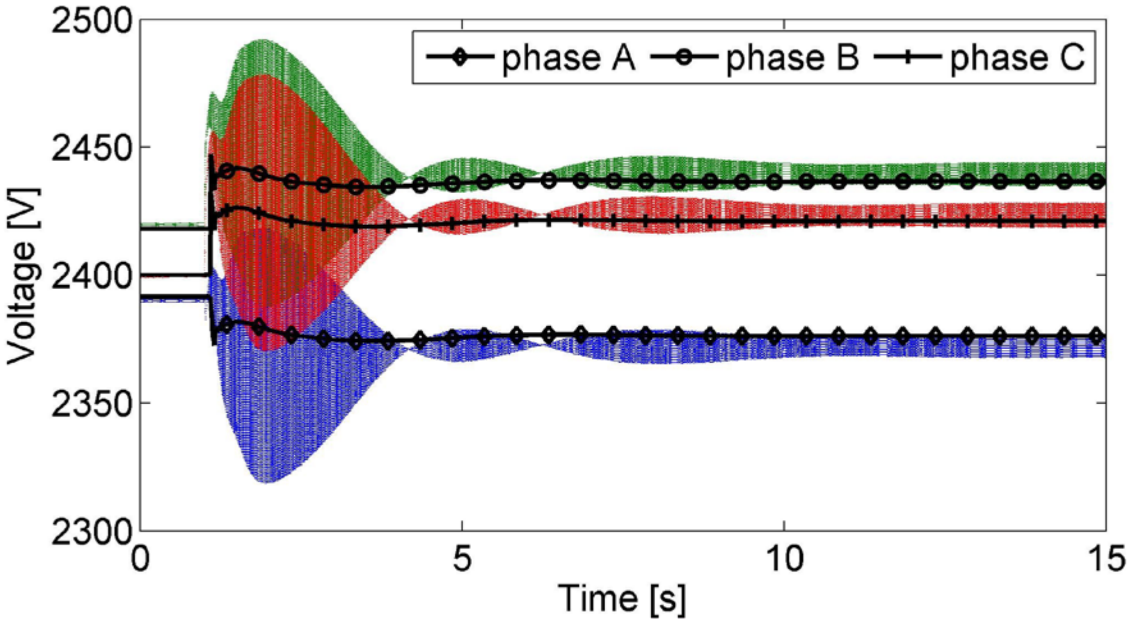

Figure 2. Three-phase voltages for sample microgrid after load-shed event

Another key aspect of the unbalanced dynamics is representing the frequency of the islanded microgrid. Figure 3 shows the same IEEE 13-node scenario presented above, but represents the mechanical speed of one generator shaft. Of note here is the deviation above 62.5 Hz. Such a large deviation may trip over-frequency relays on the generator or loads within the system, which could lead to unintended behavior. Factoring these disturbance behaviors is necessary to explore if the microgrid would continue to operator properly, or would trip off further generation or load.

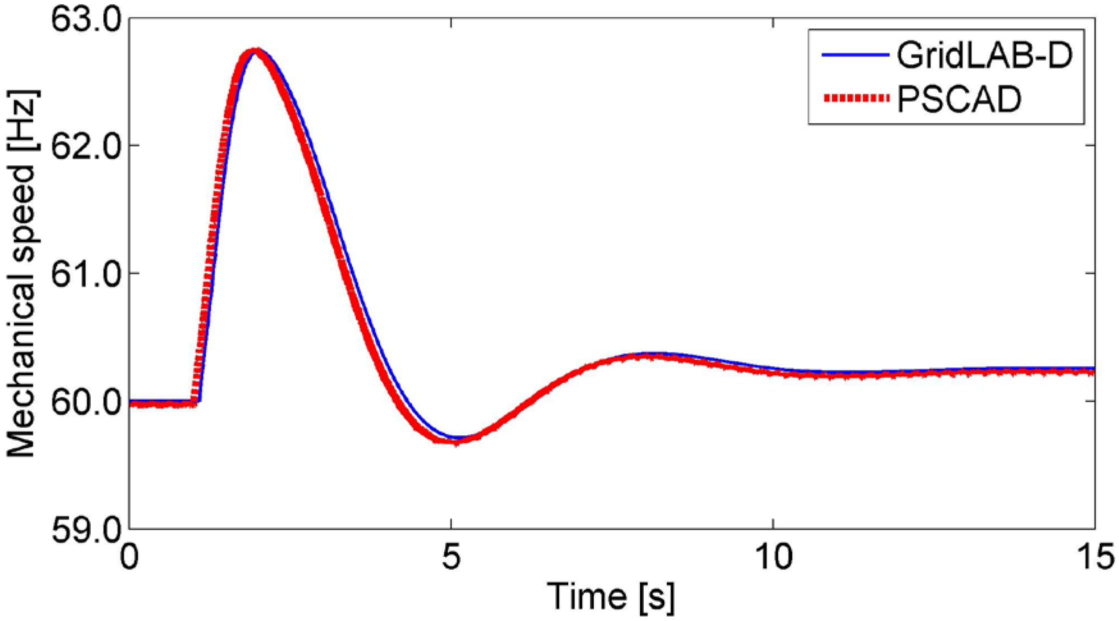

Figure 3. Mechanical speed for generator in sample microgrid after load-shed event

2.2.2 Distribution line and transformer in-rush

The basic synchronous machine and powerflow dynamics represent a key component to evaluating the feasibility of a microgrid during emergency operations. However, without the larger power capacity, higher inertia transmission system connection that typically exists for the distribution-level assets, other behaviors must also be considered. The in-rush current associated with restoring a de-energized line or transformer can often be significant. This in-rush can trip protective relays and equipment safety mechanisms, as well as momentarily overload any distributed generation on the system.

The underlying basis for in-rush is the re-establishment of any electric or magnetic fields associated with the interactions of different cables or coils within distribution lines and transformers. While the in-rush associated with charging lines and cables is typically not a concern at the distribution level, transformer in-rush can be quite significant, especially when transformer saturation occurs. A valid representation of these for the dynamic simulations of microgrids is essential, especially for the start-up portions of the microgrid, inclusion of de-energized sections, or particularly large inductive or capacitive loads.

The basis for in-rush current calculations comes from the electromagnetic equations for the lines and transformers. These equations provide highly detailed results, but often require very small timesteps and produce point-on-wave data, as opposed to the phasor-type representation many distribution power simulations provide. To resolve this issue, the electromagnetic equations are converted into a phasor-type notation known as the dynamic phasor approach [11].

The basis for the dynamic phasor approach is to convert the time-domain, differential equation into frequency-domain function that has a time-varying component. The basic equation for a dynamic phasor substitution is given by:

$$\left\langle \frac{dx}{dt} \right\rangle_k = \frac{dX_k}{dt} + j\omega_s X_k \tag{6}$$

where:

X_k	Frequency domain representation of the time domain response,
ω_s	Sampling frequency (base sampling time),
t	Time variable, and
k	Multiple of the sampling frequency.

Leveraging the dynamic phasor basis, the Shifted Frequency Analysis [12] is applied to simple lines and transformers to get the first order in-rush effects. The details of the EMTP and electromagnetic implementation can be found in [12], [13], and are omitted for brevity. The resultant equation, for distribution line in-rush is given by:

$$\mathbf{\Delta I(t) = I(t) + H(t) - G\Delta\ V(t)} \tag{7}$$

where:

$\mathbf{I(t)}$	Dynamic phasor representation of currents,
$\mathbf{H(\tau)}$	Time-varying history term for the line,
$\mathbf{G}$	Nodal equivalent admittance matrix, and
$\mathbf{V(t)}$	Dynamic phasor representation of the nodal voltages.

Implementing the base in-rush equation in this manner makes it compatible with the current-injection method referenced earlier in the paper [8]. Implementing it in this manner prevents needing to rearrange the Jacobian matrix of the powerflow solver, as well as leverage the in-rush contributions of end-use loads. However, the primary advantage to implementing the in-rush equations in this manner is the ability to model meshed or networked topologies. Many traditional in-rush implementations rely on strongly-fixed voltage sources (e.g., swing bus) and radial topologies. The current-injection-based methodology removes these restrictions, allowing simulation of a broader range of microgrids and scenarios.

When implemented on a simple distribution line with a larger, inductive load at the end, an in-rush result similar to Figure 4 is obtained. Figure 4 includes the PSCAD simulation results for verification. For ease of visual comparison, the GridLAB-D results have been scaled by the square root of two, approximating the conversion from their root-mean-square (RMS) value to the point-on-wave representation PSCAD utilizes. While the initial in-rush is not significant and only about 1/6 of the steady state value, if a protective relay had a threshold of 300 amps, energizing such a line and load could cause the system to trip this segment back out of service.

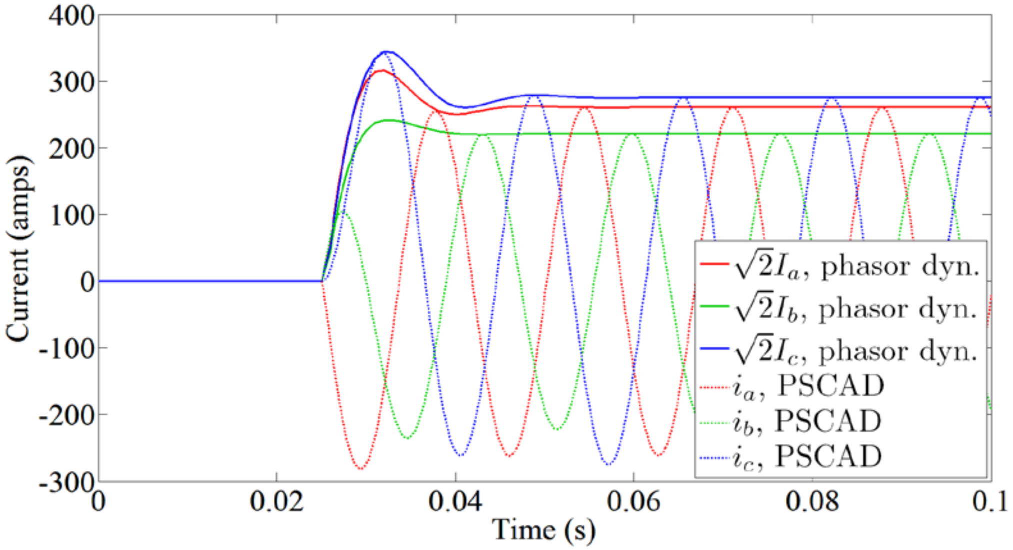

Figure 4. Simple line in-rush example

In addition to simple distribution line sets, the formulation above is also effective for modeling the in-rush associated with ideal transformers. However, if the magnetization impedance and saturation are included in the model, the results are vastly different. Without these elements, results similar to Figure 4 above occur, but these do not represent the true behavior of the transformer. The nature of a distribution transformer requires a core linking the primary and secondary windings. This coupling core can only serve as a connecting loop for only so much electromagnetic flux before hitting an upper limit. Figure 5 shows a sample saturation curve for a transformer, showing how increasing the flux beyond Φ_M starts to have decreasing gains on the current. This saturation can create much larger in-rush on the system, causing an even greater transient current and power swings that may trigger protective actions and devices.

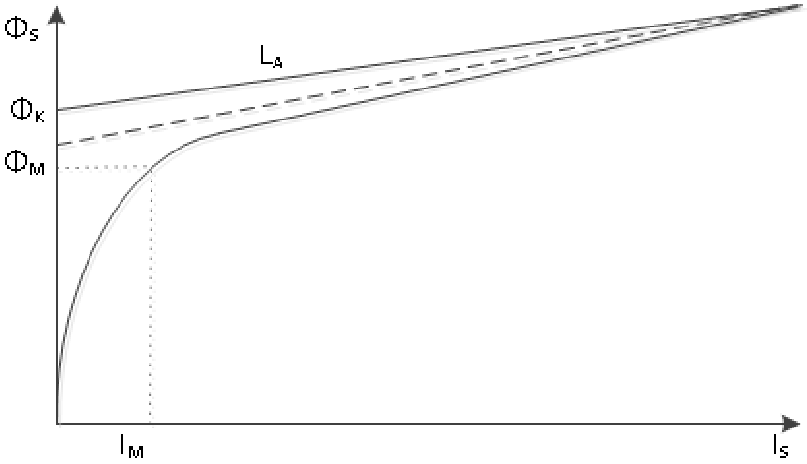

Figure 5. Sample saturation curve for transformer showing flux-to-current relationship

Incorporating this saturation curve into the transformer model requires two additional steps. The first, more straight-forward step, is implementing the base flux-to-current equations for incorporation into the current injection method. The implementation begins with the basic flux equation of [13], [14], given as

$$\frac{d\phi(t)}{dt} = v(t) - \frac{\phi(t)}{2T_D} \tag{8}$$

where:

$\phi(t)$	Time-varying flux of the transformer,
$v(t)$	Time-varying, point-on-wave voltage values, and
T_D	Magnetic damping time.

Converting this to the dynamic phasor notation, as well as incorporating a variant of the trapezoidal rule results in

$$\mathbf{\Phi}(t) = \mathbf{AV}(t) + \mathbf{H_\Phi}(t) \tag{9}$$

$$\mathbf{H_\Phi}(t) = \mathbf{A}(1+\mathbf{B})\mathbf{V}(t-\Delta t) + \mathbf{BH_\Phi}(t-\Delta t) \tag{10}$$

$$\text{with } A = \frac{2\Delta t T_D}{4T_D + j2\omega T_D \Delta t + \Delta t} \text{ and } B = \frac{4T_D - j2\omega T_D \Delta t - \Delta t}{4T_D + j2\omega T_D \Delta t + \Delta t},$$

which put the magnetizing flux in the same format as the line-in-rush utilized earlier. However, transformer in-rush currents are also highly sensitive to where the point-on-wave signal is when energized, so the "incidence" time of the flux must also be included. This is accomplished by performing a rotation of the flux in the phasor domain, and then applying the saturation function. This rotation is included using the two equations,

$$\phi_P(t) = abs(\phi(t))\sin(angle(\phi(t)) + \omega t \tag{11}$$

$$I_S = \frac{\left(abs(\phi_{p,t_i}) - \Phi_K\right)^2 + 4DL_A + abs(\phi_{p,t_i}) - \Phi_K}{2L_A} - \frac{D}{\Phi_K} \tag{12}$$

$$\text{with } D = -\frac{B - \sqrt{B^2 - 4AC}}{2A},\ A = \frac{L_A}{\Phi_K^2},\ B = \frac{L_A I_M - \Phi_M}{\Phi_K}, \text{ and}$$

$$C = I_M L_A I_M - \Phi_M + \Phi_K$$

where:

L_A	Air core inductance,
I_M	Peak magnetization current at rated voltage,
Φ_K	Knee flux value from Figure 5, and
Φ_M	Peak magnetization flux from Figure 5.

With the addition of equations (9) to (12), the saturation impacts of the transformer core are captured and used to influence the in-rush currents. Figure 6 shows the primary side currents to a variation of the IEEE 4-node system when the system is switched into a larger, transmission system. Due to the nature of the unbalanced load at the end of the test feeder, the different phases experience the saturation impacts at different intervals. The worst saturation occurs on phase a of Figure 6, with the in-rush current reaching a peak magnitude of almost three times the steady state value. Without accounting for this impact, such a large in-rush could easily trigger protective devices or cause an undesired response in the generator of a microgrid.

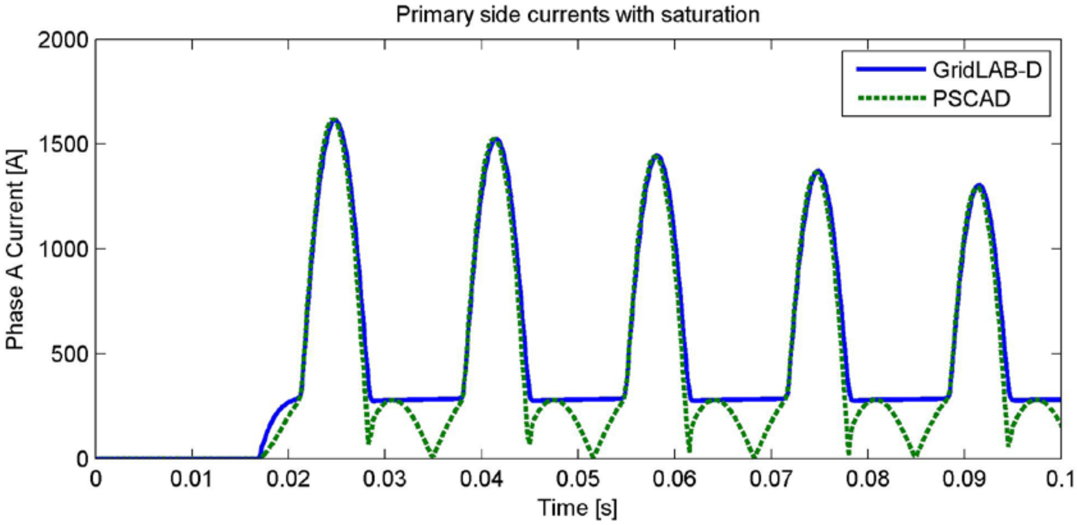

Figure 6. Primary currents for saturated transformer during in-rush scenario

2.2.3 Resilience-Oriented Service Restoration and Reconfiguration

In addition to the dynamic considerations to use Microgrids as a Resiliency Resource, the fundamental connections between sections of the distribution grid are also important. During an outage, the power connections between portions of the distribution system can be energized by the microgrid to provide power to a greater region. Some guidance must be provided on this reconfiguration approach, such as which switches to manipulate and which loads are critical. As indicated earlier, due to the limited capacity of distributed generators (DGs) within microgrids, dynamic performance of the DGs during this restoration process becomes essential. The stability of microgrids, frequency deviation, and transient voltages and currents of DGs are considered as constraints during the restoration of critical load. By introducing the concepts of restoration tree and load group, the critical load restoration problem is transformed into a maximum coverage problem, which is a linear integer program. The restoration paths and actions are determined for critical loads by solving the LIP.

2.2.3.1 Problem Formulation

Assume that after a major disaster, faulted zones are isolated and microgrids are operated in an islanded mode. As a result, interrupted islands are formed. An *interrupted island* is a normally connected portion of a distribution feeder, which has no connection (except open switches) to other portions of the system, and has no power source within it. Microgrids and interrupted islands are linked by tie switches or microgrid switches. A microgrid will first serve critical loads within it. If the microgrid has remaining generation capacity, it is considered an available source for service restoration of critical loads on the distribution feeders. An example of the post-event structure of a distribution system is shown in Figure 7.

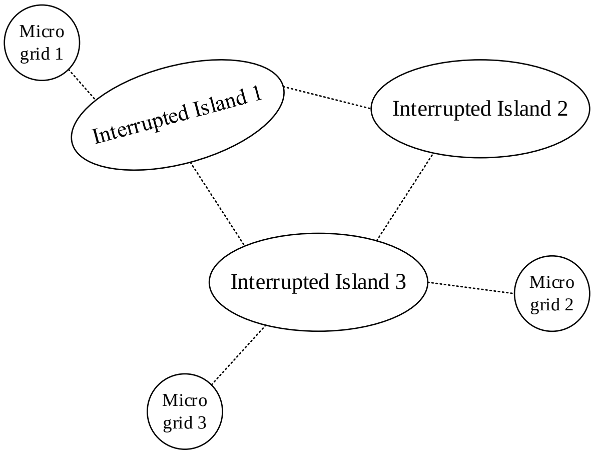

Figure 7. Post-event structure of a distribution system

A weighting factor is assigned to each zone with critical loads to represent the priority level. The objective is to maximize the weighted number of critical loads restored. Critical loads within the microgrid and in the interrupted portion are considered. However, critical loads within the microgrid are prioritized – they won't be disconnected, unless a much more critical load needs to be picked up. Also note that non-critical loads that cannot be disconnected from the paths between power sources and critical loads by switching operations will also be energized when the critical loads are restored. Power generation resources, such as diesel and natural gas, are limited after a major disaster, so the amount of non-critical load energized should be minimized. Dynamic, operational, and topological constraints are considered utilizing methods described earlier in this report. The critical load restoration problem is formulated as follows.

Objective Functions:

1) Primary objective: Maximizing the weighted number of critical loads restored, i.e.,

$$\max \sum_{i \in \mathbf{Z}_{cri}} x_i c_i N_i \tag{13}$$

where $\mathbf{Z}$ is the set of all loads, critical ($\mathbf{Z}_{cri}$) and non-critical ($\mathbf{Z}_{uni}$), x_i is the weighting function, and c_i is the ith critical load priority level, and N_i is the critical load value.

2) Secondary objective: Minimizing the amount of non-critical load that are energized, i.e.,

$$\min \sum_{i \in \mathbf{Z}_{uni}} x_i p_i^{nc} \tag{14}$$

where p_i is the ith non-critical load value.

Constraints:

Note that all constraints within this section are for the scenarios simulated and are taken as a best practice for the systems simulated. In a full utility restoration scenario, individual limits for the different dynamic constraints may be adjusted, based on utility load composition and operating practices.

1) Dynamic Constraints: Assume that the restoration process starts at time $t = 0$ and ends at time $t = T > 0$. The entire system reaches a steady state at time $t = T$ (if it is stable).
   - Each microgrid must be stable during the restoration process.
   - During the restoration process, the frequency of each microgrid should be within an acceptable range, i.e.,

$$f_{\min} \le f_k(t) \le f_{\max}, k \in \mathbf{M}, t \in [0, T] \tag{15}$$

where f represents the frequency and **M** is the set of individual microgrids. Here, the nominal frequency is 60 Hz and the acceptable range of transient frequency is [54, 62] Hz. This is a fairly wide frequency band, meant to show just how much load can be picked up during reconfiguration steps. This may be a much tighter band in different scenarios, particularly if any loads or generators have more constrained under-frequency protective devices.

   - The transient voltages at the terminal of generators should not exceed the preset limits, i.e.,

$$V_{\min}^{tr} \le V_g^{tr}(t) \le V_{\max}^{tr}, g \in \mathbf{G}, t \in [0, T] \tag{16}$$

where V is the generator terminal voltage and **G** represents the set of all generators on the system. Here, $V_{min}^{\mathrm{tr}} = 0.9$ p.u. and $V_{\max}^{\mathrm{tr}} = 1.1$ p.u..

   - The transient currents output by a generator should not exceed the preset limits, i.e.,

$$I_g^{tr}(t) \le I_{\max,g}^{tr}, g \in \mathbf{G}, t \in [0, T] \tag{17}$$

where I is the generator output current. Here, $I_{\max,g}^{\mathrm{tr}}$ is 1.1 times of the nominal current.

2) Operational Constraints:
   - Unbalanced three-phase power flow equations [18] must be satisfied.

$$P_u^s - jQ_u^s = \left(\overline{V}_u^s\right)^* \sum_{v \in \mathbf{\Omega}_u} \sum_t Y_{uv}^{st} \overline{V}_v^t, u \notin \mathbf{\Omega}, s, t \in \{a, b, c\} \tag{18}$$

with P and Q representing real and reactive power components, Y representing the equivalent shunt admittance of a node, and $\mathbf{\Omega}$ representing the set of all nodes on the system.

   - Steady-state bus voltages within the microgrid should be maintained within acceptable operating limits.

$$V_{\min} \le V_u \le V_{\max}, u \in \mathbf{\Omega} \tag{19}$$

For these scenarios, $V_{\min} = 0.95$ p.u. and $V_{\max} = 1.05$ p.u. Note that this is a fairly tight range of operation and could be relaxed, depending on specific feeder and utility constraints.

   - Steady-state line currents should not exceed their limits.

$$I_l \le I_{\max,l}, l \in \mathbf{L} \tag{20}$$

   - The steady-state output power of each microgrid should not exceed the maximum amount of power that it can provide, i.e., the total generation capacity of DGs minus the amount of critical load within the microgrid.

$$\begin{cases} P_k \le P_{\max,k} \\ Q_k \le Q_{\max,k} \end{cases}, k \in \mathbf{M} \tag{21}$$

3) Topological Constraint:
   - The radial structure of the network should be maintained, i.e., a critical load is served by only one microgrid through only one path and the paths for different critical loads do not overlap. Maintaining the radial structure will help avoid some operational issues, such as load sharing among microgrids. Moreover, in a radial network, the relay settings are easier to adjust to protect the system from potential subsequent faults.

2.2.3.2 Solution Method

A four-step procedure is proposed to determine the critical load restoration strategy: 1) construct restoration trees, 2) form load groups, 3) formulate and solve the critical load restoration problem as a maximum coverage problem, and 4) determine restorative actions.

The first step identifies the paths from microgrids to critical loads. Regard a zone with critical load as a critical load zone. For each “microgrid – critical load zone” pair, a unique path is determined, which is called a restoration path, or there is no feasible path between them. All paths starting from a microgrid form a graph-theoretic tree rooted at the microgrid, referred to as a restoration tree. The number of restoration trees is equal to the number of microgrids.

The second step is to form the load groups. A load group is a subset of load zones that can be restored together by a microgrid through their restoration paths. For each microgrid, a set of load groups can be determined from its restoration tree. If a load zone belongs to a load group, it is covered by the load group.

The third step formulates the critical load restoration problem as a maximum coverage problem. By solving the maximum coverage problem, the set of critical load zones restored and the set of load groups covering these critical load zones are determined. The corresponding restoration paths are identified from the restoration trees.

The last step determines the restorative actions, i.e., switching operations, to restore the critical loads. Dynamic simulations are performed to evaluate the feasibility of the actions.

2.2.3.3 Case Study – 1069-bus model

A 4-feeder 1069-bus test system with four microgrids and five critical loads is used to validate the effectiveness of the proposed method. The one-line diagram of the test system is shown in Figure 8. The test system has a model in a GridLAB-D compatible format, which is based on the taxonomy feeder “R3-12.47-2” model developed available on the GridLAB-D website [4].

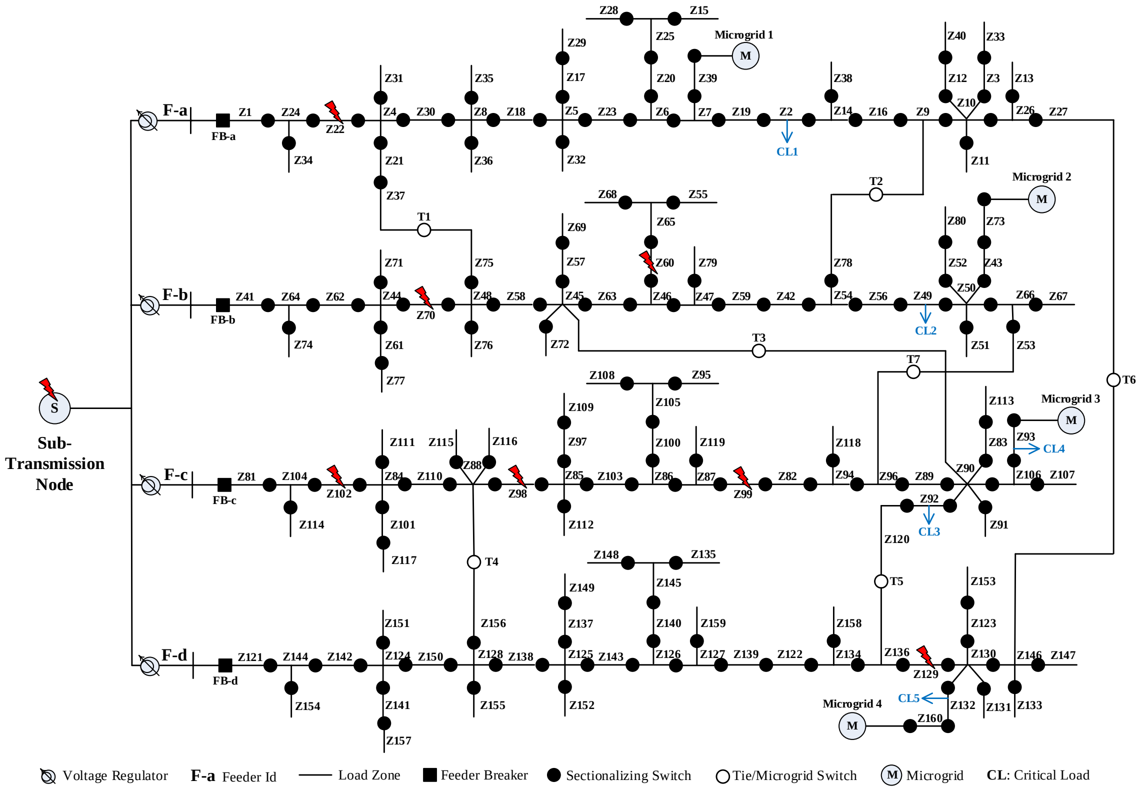
F-a
F-b
F-c
F-d
FB-a
FB-b
FB-c
FB-d
S
Sub-Transmission Node
Microgrid 1
Microgrid 2
Microgrid 3
Microgrid 4
M
CL1
CL2
CL3
CL4
CL5
T1
T2
T3
T4
T5
T6
T7
Voltage Regulator
F-a Feeder Id
Load Zone
Feeder Breaker
Sectionalizing Switch
Tie/Microgrid Switch
M Microgrid
CL: Critical Load

Figure 8. One-line diagram of a 4-feeder 1069-bus test system

A simplified microgrid model is used in this study, as shown in Figure 9. Each microgrid is modeled as a grid with a single bus. An aggregated generator, whose capacity equals the total capacity of controllable units, and an aggregated load, representing critical loads, are connected at the bus. The generator model described earlier, applicable for unbalanced simulation, is utilized. A Woodward diesel governor model and a simplified exciter system model are used for the controllers of generators. The microgrid is connected to the distribution system through a transformer at the point of common coupling (PCC). The generation capacity and load information for the four microgrids in the test system are given in Table 1. The power factor of microgrid loads is given as 0.9.

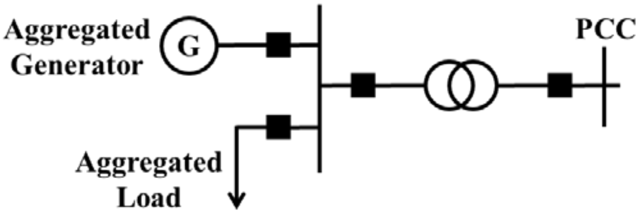
Aggregated Generator
G
PCC
Aggregated Load

Figure 9. A simplified microgrid model

Table 1. Generation Capacity and Load Data for Microgrids

Microgrid ID	1	2	3	4
Generation Capacity (MW)	10	5	7	4
Critical Load (MW)	4.38	2.1	2.95	1.86

Five zones in the test system are critical load zones, i.e., Z2, Z49, Z92, Z93, and Z132. Each zone contains one critical load, whose priority levels (i.e., c_i) are 3, 3, 2, 2, and 1, respectively. Assume that an extreme event caused an outage of the entire distribution system. Power from the transmission system is unavailable. Seven faults occurred in the distribution network. The faulted zones are Z22, Z60, Z70, Z98, Z99, Z102, and Z129, as shown in Figure 8. Detection of these faulted zones is outside the scope of this restoration algorithm. It is assumed faulted sections will be detected via an outage management system, or some form of direct observation.

The proposed method is used to find a restoration strategy for the critical loads. First, restoration trees of the four microgrids are constructed. The results are given in the form of restoration paths, as shown in Table 2.

Table 2. Restoration Trees

Microgrid ID	Restoration Paths
1	1) M1-Z39-Z7-Z19-Z2 2) M1-Z39-Z7-Z19-Z2-Z14-Z16-Z9-Z78-Z54-Z56-Z49 3) M1-Z39-Z7-Z6-Z23-Z5-Z18-Z8-Z30-Z4-Z21-Z37-Z75-Z48-Z58-Z45-Z90-Z92 4) M1-Z39-Z7-Z6-Z23-Z5-Z18-Z8-Z30-Z4-Z21-Z37-Z75-Z48-Z58-Z45-Z90-Z106-Z93 5) M1-Z39-Z7-Z19-Z2-Z14-Z16-Z9-Z10-Z26-Z27-Z146-Z130-Z132
2	None
3	1) M3-Z93-Z106-Z90-Z45-Z63-Z46-Z47-Z59-Z42-Z54-Z78-Z9-Z16-Z14-Z2 2) M3-Z93-Z106-Z90-Z45-Z63-Z46-Z47-Z59-Z42-Z54-Z56-Z49 3) M3-Z93
4	None

Sixteen load groups are formed, as shown in Table 3. Only critical load zones in each load groups are given. Non-critical load zones in the load groups can be identified from the restoration paths given in Table 2.

Table 3. Load Groups

Index *j*	Source	Critical Load Zones	Non-Critical Load (MW)
1	Microgrid 1	Z2	0.4752
2	Microgrid 1	Z92	1.9616
3	Microgrid 1	Z93	1.9616
4	Microgrid 1	Z92, Z93	1.9616
5	Microgrid 1	Z2, Z132	2.5772
6	Microgrid 1	Z2, Z93	1.9616
7	Microgrid 1	Z2, Z92	1.9616
8	Microgrid 1	Z2, Z49	0.6775
9	Microgrid 1	Z2, Z92, Z93	1.9616
10	Microgrid 1	Z2, Z49, Z132	2.5936
11	Microgrid 1	Z2, Z49, Z93	2.1639
12	Microgrid 1	Z2, Z49, Z92	2.1639
13	Microgrid 1	Z2, Z49, Z92, Z93	2.1639
14	Microgrid 3	Z93	0
15	Microgrid 3	Z49, Z93	1.6984
16	Microgrid 3	Z2, Z93	1.5126

Dynamic simulations are essential in the evaluation of feasibility of load groups. For example, from Figure 8, it can be seen that microgrid 4 is close to critical load CL5. It seems like a good idea to use microgrid 4 to restore critical load CL5 through path “M4-Z160-Z132.” By performing a power flow calculation, one can find that the path does satisfy all operational constraints. However, it is not listed as a feasible restoration path in Table 2. This is because the amount of load on zone Z160 is large and the generator capacity of microgrid 4 is relatively small, which causes instability when microgrid 4 tries to pick up zone Z160. This is not due to the steady-state rating of the equipment, but rather the transient associated with the load pickup; this transient would exceed the operational limits for the microgrid and protective devices would activate on the microgrid, preventing the load from being energized.

The critical load restoration problem is formulated as a maximum coverage problem and solved. Load groups 12 and 14 are selected. Four out of five critical loads are restored. Specifically, zones Z2, Z49, and Z92 are restored by microgrid 1, zone Z93 is restored by microgrid 3, while zone Z132 remains interrupted. The total amount of non-critical load energized is 2.1639 MW.

Finally, restorative actions are determined. After disconnecting load zones that are not on the restoration paths, critical load zones Z2, Z49, and Z92 are restored by microgrid 1 in three actions, while Z93 is restored by microgrid 3 in one action. The time interval between two consecutive actions is set as one minute. The transient frequency of the two microgrids is shown in Figure 10.

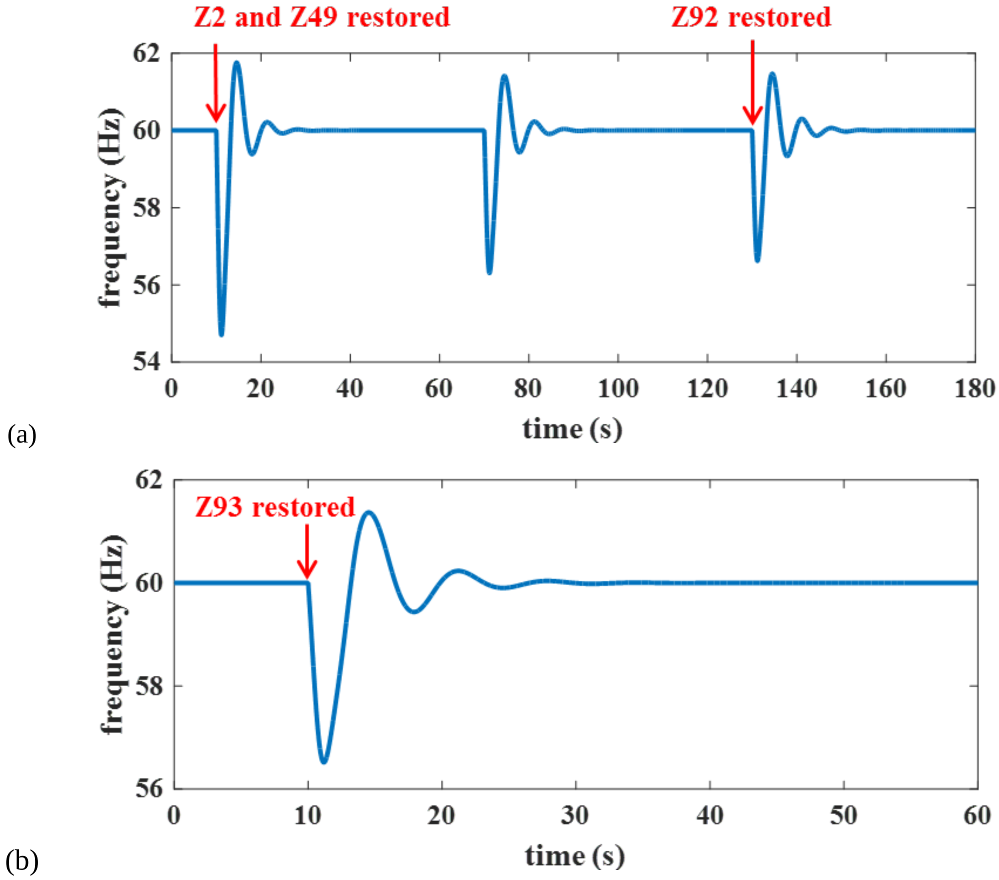

Figure 10. Transient frequency of (a) microgrid 1 and (b) microgrid 3

2.2.3.4 Case Study – Pullman-WSU Distribution System

For the second case study, a more realistic scenario is examined on the Pullman, Washington and Washington State University (WSU) grids. There are two critical loads on the Pullman distribution feeders, both serviced by the larger distribution system managed by Avista Utilities: the Pullman Regional Hospital, and the Pullman City Hall (acting as a local emergency response center). Three generators are installed on the WSU campus: one 1.75 MW diesel generator, and two 1.1 MW natural gas generators. These generators serve as the potential power sources for service restoration when power from Avista is unavailable.

Suppose a severe event occurred at the South Pullman 115 kV substation. As a result, the five feeders served by the substation are out of service. Moreover, no power source in the Avista system is available at the time. A restoration plan is obtained by applying the proposed method, as shown in Figure 11. The WSU generators first pick up three critical loads on campus, and then restore the City Hall and Hospital through a restoration path with one transformer and nine zones. The restoration plan is implemented in seven steps. The time interval between two restorative actions is assumed to be one minute. In steps 1-3, critical loads within WSU are restored. Steps 4-7 restore the loads on the restoration path. The City Hall and Hospital are restored in step 5 and 7, respectively. The curves of system frequency and generator voltages from the reconfiguration simulation are shown in Figure 12. Note that a Woodward diesel governor model with a droop speed control (DEGOV1) is applied to allow proper load sharing among the three generators. The secondary frequency control is not considered. Therefore, the steady-state frequency is a little bit lower than 60 Hz.

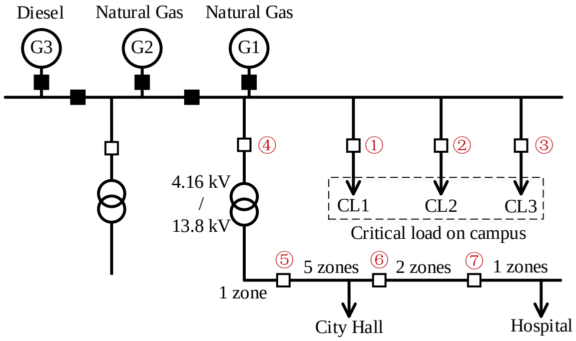
Diesel
Natural Gas
Natural Gas
G3
G2
G1
④
①
②
③
4.16 kV
/
13.8 kV
CL1
CL2
CL3
Critical load on campus
⑤
5 zones
⑥
2 zones
⑦
1 zones
1 zone
City Hall
Hospital

Figure 11. Critical load restoration strategy for Pullman-WSU system

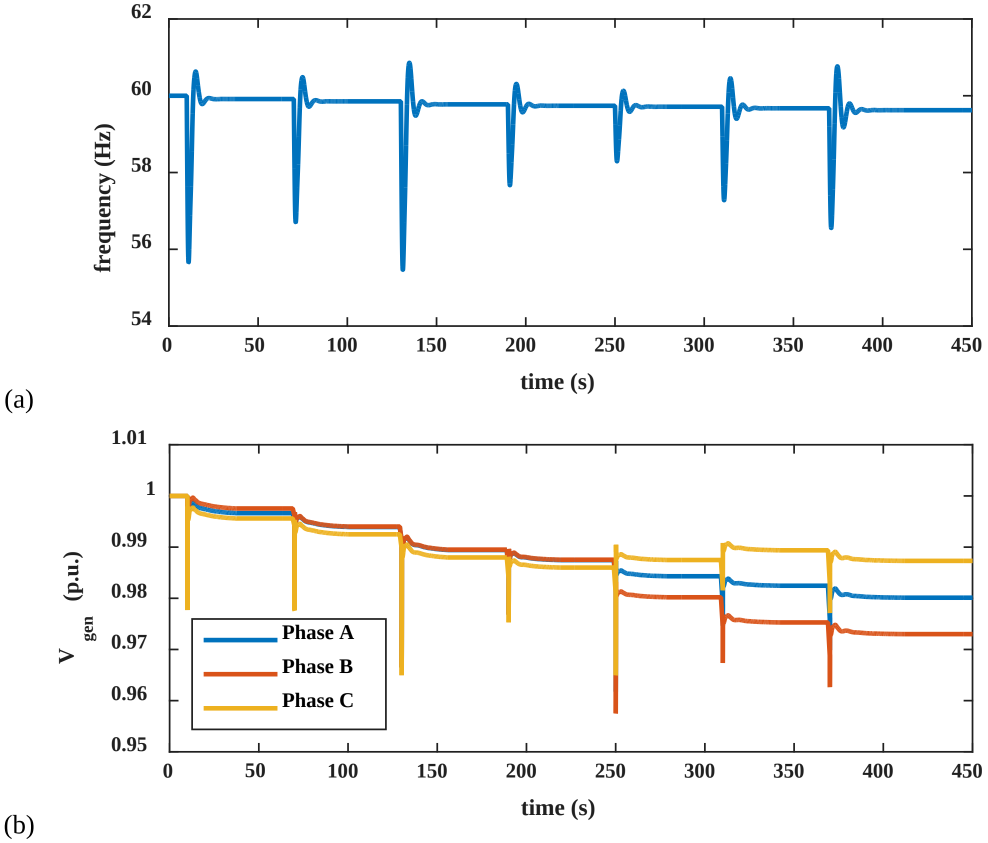

Figure 12. Curves of (a) system frequency and (b) generator voltages

2.2.4 Nomograms

During extreme events, the ability to run detailed simulations for each operating case is not always feasible. Look-up tables and rough guidelines or intuition are often utilized to energize assets, and to determine the feasibility of connections. While this can allow assets to be brought back into service and loads picked up, it may not utilize the microgrid assets to their full potential, or provide useful information beyond a simple local resource application. To address this short-coming, simulations of various conditions of a microgrid system and resources are conducted prior to the event, to create an overall nomogram of operational characteristics.

In a simple sense, a nomogram is a figure showing regions of feasible operation. Input characteristics are usually applied to the *x*-axis and *y*-axis of a two-dimensional plot. The corresponding Cartesian point is examined to see if it is above or below a particular threshold of operation. The overall method provides a quick visual analysis of a device's capabilities and indication of its feasibility of operation at that point. The regions dictated on the nomogram are often extrapolated from several simulations or field tests of the device of interest.

To demonstrate how an operational nomogram may be formed for use in microgrids, first consider a sample system. A variant of the Pullman, Washington system described in the previous section is utilized to examine the dynamic limitations of three of the WSU campus backup generators. A notional diagram is shown in Figure 13. This notional system has three backup generators, one 2.10 MVA diesel and two 1.75 MVA natural gas reciprocating generators, and a model of the WSU campus and nearby Pullman feeder infrastructure. Two critical loads are the Pullman hospital and city hall, which serves as the disaster relief center for Pullman.

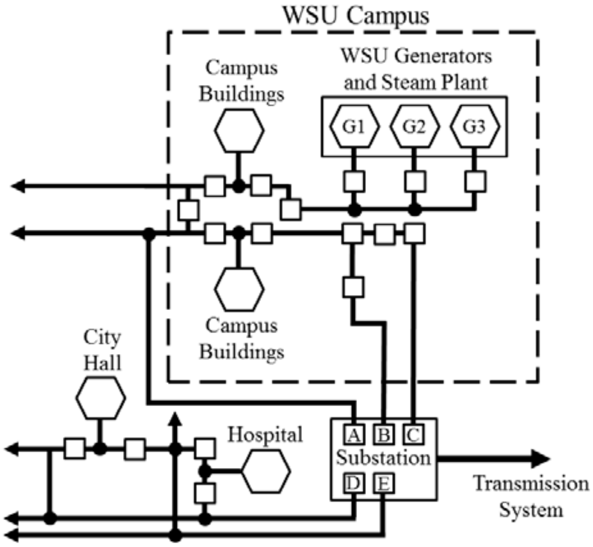

Figure 13. Notional diagram of Pullman system for simulation

Nomograms can be built upon various aspects of the operation, including dynamic responses to loads and the in-rush capabilities or consequences of switching in a transformer or line. As a simple case, consider the frequency responsiveness of different generator set operations on the model Pullman system. Consider the scenario where the diesel generator and one natural gas generator are operating on the system. Various loads are switched into the system and the frequency deviation to the step load increases are recorded, as shown in Figure 14. These values are fed into the set of values used to construct the nomogram representation shown in Figure 15. The lowest frequency of each loading case from Figure 14 is recorded, and represents a point on the corresponding line in Figure 15.

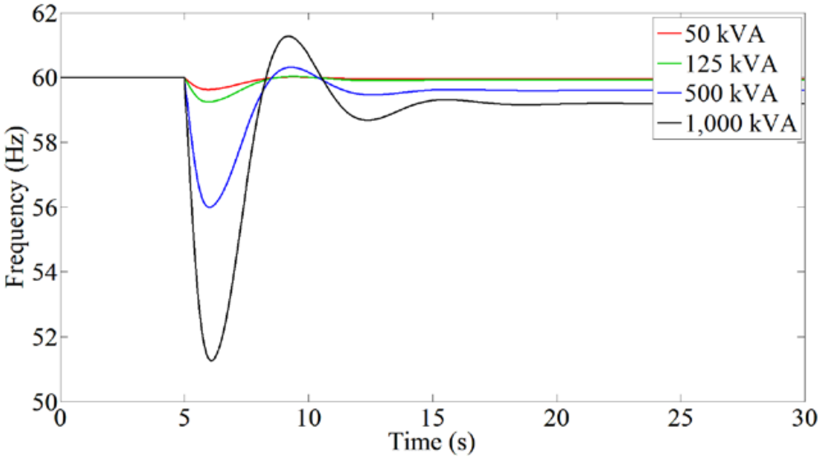

Figure 14. Frequency response for two generators to various step load changes

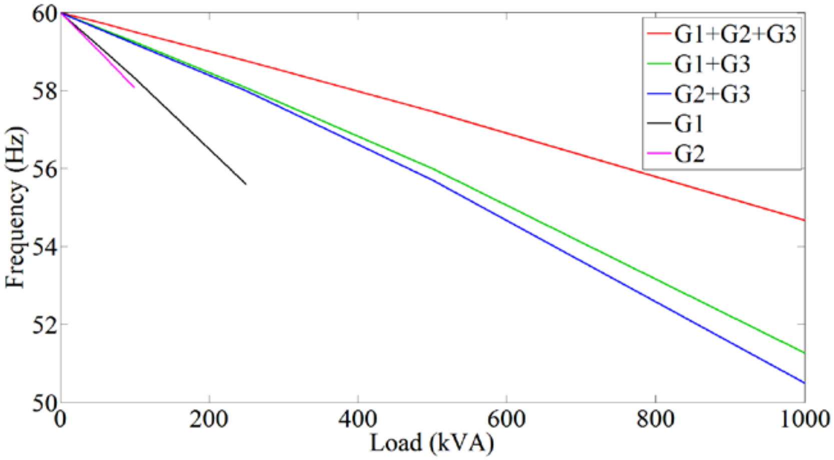

Figure 15. Sample nomogram for frequency deviations of different generator combinations

The simulations of Figure 14 represent the G1+G3 scenario in Figure 15. Notice the low frequency value of approximately 51 Hz during the 1000 kVA load switch is the lower limit of the green line in the nomogram. This particular line can be used in a variety of ways. For example, if a load of 800 kVA is needed, the corresponding frequency deviation is expected to be down to below 54 Hz for the G1+G3 combination. Furthermore, if a deviation down to 56 Hz is the only allowable range, the G1+G3 line indicates a load up to approximately 500 kVA can be switched into service.

While the example provided only shows the frequency response of the generator sets to step load changes, this type of analysis and nomogram can be conducted for a multitude of conditions and variables. Performing these bulk simulations offline provides the data to form the nomograms similar to Figure 15, which could easily be printed and made available to microgrid managers or disaster relief managers during major events.

2.3 Consolidated approach

Maximizing the potential of microgrids as a resiliency resource requires the combination of all of the approaches and methods in this chapter. With different distributed resources and capabilities in microgrid systems, the dynamics of the system change significantly, especially in unbalanced conditions. Examining these effects allows the evaluation of different operating scenarios, including load pickup events and the reconfiguration approaches described. Many approaches in journals and academic papers only consider the overall power balance of microgrids, neglecting the transient effects that may temporarily overload the generators or trigger protective devices. Fully modeling and simulating these effects allows more accurate sizing and control of the assets, as well as ensuring an infeasible scenario is not selected for operating the microgrid.

All of the simulation approaches and reconfiguration methods can be performed in advance of a major disaster or outage event. The boundaries of these scenarios, and the sequencing of switches, can all be consolidated into operational guidelines and nomograms for use by emergency personnel. These procedures can either be post-outage steps to restore power to key infrastructure, or pre-emptively isolating the system into local or community microgrids to prevent outages in service caused by larger, transmission system outages, increasing the overall resiliency of the system. The operational guide should help restore and maintain power to critical social infrastructure, such as local hospitals and disaster relief centers.

Utilizing the nomogram approach, or even near-term simulations, the feasibility of microgrids to providing larger services can be evaluated. Microgrid operations for resiliency can be divided into three overall categories for this research: use as a local resource, as a community resource, and as a black start resource. The rough configuration and considerations of each of these uses vary, but are all constrained by the more complicated dynamics and restrictions of operating a microgrid, instead of a transmission-connected system.

The first scenario is using microgrids as a local resource. This is the traditional usage, with the distributed generation serving either a single building, or a very small set of buildings as a backup generator. Depending on the building complexity, some of the unbalanced dynamics and in-rush components may need to be considered, either through the use of nomograms or simulations. In the majority of cases, the generation is sized appropriately or over-sized, providing little concern for these considerations.

Manipulating the existing distribution system and appropriate switchgear, the distribution generation can also provide benefits to a larger scenario, becoming a community resource. In the Pullman example earlier, the Pullman distribution grid is reconfigured such that the generators on the WSU campus can provide additional backup power to the local hospital and city hall. When using microgrids in a community resource configuration, the impacts of the unbalanced dynamics, generator restrictions, and in-rush considerations become more pressing. Picking up large sections of load can overwhelm generators and potentially cause them to trip due to under-frequency or under-voltage protection. Utilizing the reconfiguration approach outlined earlier, along with the nomogram approach or dynamic simulations, the distribution system can be adjusted to successfully get power from the distributed generation to the desired end load. Consulting the simulation constraints or the nomograms ensures the generators are not overloaded during this reconfiguration and allows resources beyond the immediate microgrid to benefit from the available power.

The final scenario for microgrid use can be as a black start resource. Larger thermal plants do not start instantaneously after a large blackout, and often require external power to start the various power generation processes. Certain power plants are included in black start plans, containing on-site backup generation to help restart the plant. A power plant may not be considered in these plans due to location, or even due to the expense of adding and maintaining the on-site backup requirements. The plant could also be the only major thermal plant on a portion of the transmission grid, if the cause of the outage caused more widespread damage to infrastructure (e.g., earthquake). If a microgrid were located sufficiently close to such a power plant, it could provide the capability to start part of the plant, restoring the overall transmission service in a timelier manner. While dynamics and generator loading become more significant in this scenario, two main restrictions limit a microgrids use as a black start resource: reactive power capability and in-rush currents.

When energizing higher-voltage, longer transmission-system power lines, more reactive power is required to maintain the voltage levels. Under the right circumstances, especially unloaded, these transmission lines may even appear to produce reactive power, which must be sinked by the distributed generator. The ability to both produce and absorb significant portions of reactive power can be beyond the capabilities of the distributed generation source.

The operational nomogram approach is very useful for this analysis, especially in the evaluation of different voltage levels and line lengths. Figure 16 shows a sample under the same test system from Figure 13, but energizing a variety of transmission lines. The nomogram of Figure 16 allows a quick evaluation that even with all three generators, a 25 mile-long 115 kV line could not be successfully energized, preventing the microgrid from serving as a black start resource at that distance.

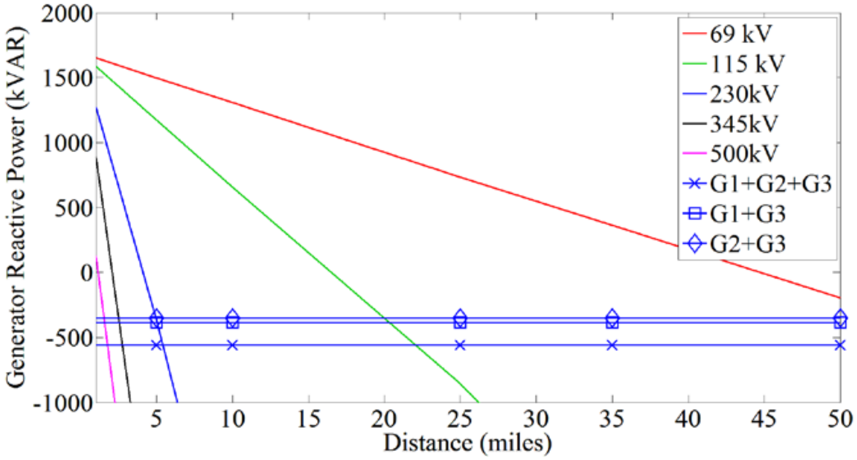

Figure 16. Example reactive power nomogram for different transmission line lengths, voltage levels, and generator capabilities

The other major restriction on microgrids as a black start resource is on the in-rush current associated with not only the transmission lines, but also the distribution-to-transmission step-up transformers. As was shown in Figure 6 earlier, if the system is saturating the transformer during the initial start-up, this can be especially limiting. Extensive simulations, or nomograms indicating in-rush capabilities of the generators for different transformer sizes and voltage changes, are needed to successfully evaluate the feasibility of energizing portions of the transmission system.

Depending on the needs of the community, the severity of the disaster, and the capabilities of equipment, microgrids can serve a variety of roles in helping to either maintain power, or restore service to areas faster. This extends all the way from local resources in a single building, to providing black start capabilities for a nearby thermal plant. Under all scenarios, the dynamics of operating the generator at the distribution level and lower equipment capabilities require careful planning and consideration for operation. With appropriate simulations or nomograms in hand, local generation assets can be utilized to form the different microgrid scenarios and provide great benefit to restoring or maintaining power in an area after a major event.

3.0 Distribution-level State Estimation and Parameter Estimation

Electric distribution systems have historically lacked measurement points, and equipment is often operated to its failure point. The failure of the equipment, as well as natural fault instigators like line-to-line tree strikes, can often resulting in customer outages. The widespread deployment of sensors at the distribution level, including measurements from Advanced Metering Infrastructure (AMI), is enabling observability into the distribution system. This observability enables the tracking of the state of distribution system equipment over time. A system can be developed using the AMI data that is transmitted to the utility to carry out State Estimation (SE) and Parameter Estimation (PE) of system model parameters such as the resistance of cables and connections. These tracked equipment parameters could then be integrated into a larger asset management system that will allow utilities to determine when proactive replacement of equipment is warranted. This system would increase the system reliability and resiliency by reducing unplanned outages, and reduce costs by only replacing equipment when appropriate.

3.1 Background and Introduction

Increasing demands on the nation’s electric infrastructure have resulted in reduced operating margins and greater stress on individual components [15]. The trend in increasing operational demands is especially acute at the distribution level where many of the emerging smart grid technologies are being deployed [16]. Continually increasing load and new load behaviors are leading to systems that are operating closer to their operational limits [15]. Operating with reduced operating margins can be done effectively if system operators have an accurate view of the current system conditions; at the transmission level this is done with state estimators. The output of the SE is used as the input to numerous other functions, such as security constrained dispatch, that give system operators the visibility they need to operate in a system with reduced operating margins [17].

Historically, electric distribution systems have lacked observability and equipment has been operated to the point of failure, resulting in temporary loss of load while repairs or replacements are carried out. One example is a cable splice failure, in which joints that are made between cables on the primary of a distribution feeder degrade over time and then either fail to maintain conductance along the line or short to ground after the insulation degrades [18]. Techniques have been developed to anticipate these failures, including field measurements of temperature [19] or waveform monitoring [20], but they require the deployment of additional equipment, and are time-consuming and expensive. Other examples of equipment failure that will result in a change of series impedance values over time include breaker contact degradation and transformer shorting. The degradation of breaker contacts over time due to arcing leads to growing impedance and eventual failure. Transformers that are operated above their power rating can experience pinpoint insulation breakdown, resulting in a short between adjacent windings. All of these equipment failure mechanisms may be foreseen by a process that can track series impedance parameter values over time, which could result in reduced customer outage time and increased reliability.

Schweppe’s concept of state estimation for electric power systems, first published in 1970, is based on a maximum likelihood Weighted Least Squares (WLS) formulation for the transmission state variables [21]–[23]. The output of state estimation gives the maximum likelihood values of the state values.

Because of measurement errors, gross topological errors, and parameter errors, the estimated values will differ from the actual values [24]. Measurement errors are addressed by assuming a Gaussian distribution, and gross topology errors can be addressed by a topology processor [24]. Parameter errors in the underlying system model that is used by the state estimator can be identified with multiple methods [25]–[27].

Operational state estimation has been until recently largely limited to transmission systems due to the low number of measurements at the distribution level, which results in an unobservable system. Despite the lack of extensive Supervisory Control And Data Acquisition (SCADA) measurements, the concept of Distribution System State Estimation (DSSE) was introduced in [27] and developed further in [28]–[32]. The work in [27]–[32] was based on a limited number of SCADA measurements and the extensive use of pseudomeasurements and end-use load estimates.

The deployment of Automatic Meter Infrastructure (AMI) presents a new opportunity for DSSE. Initial uses of this data have already been explored in [28], where average load data was used in conjunction with SCADA data. Furthermore, multiple utilities have begun to implement interconnections of their AMI systems with their operational Distribution Management Systems (DMS). The integration of AMI into the operational DMS environment, combined with the expanded measurement capabilities of smart meters, allows for the potential of a DSSE with capabilities similar to the state estimators used for transmission systems. While the necessary infrastructure only exists at a small number of utilities today, it is realistic to expect that industry will continue to trend towards systems that integrate AMI into real-time control environments [33]. A DSSE can be built upon by adding PE functions.

PE requires the same measurement set and system model as SE and builds on SE algorithms [24], [34]. First proposed in 1974 [35], the technique of augmenting the state vector with a set of suspect parameters has been widely studied [36]–[40]. An alternate approach makes use of normalized measurement residuals [41]–[44], a byproduct of the SE procedure.

PE calculations are sometimes limited by low measurement redundancy or measurement noise. The accuracy and robustness of PE procedures can be improved by using the combined information from multiple measurement snapshots, e.g., consecutive SCADA samples, in a single PE. This technique has been successfully applied at the transmission level to a measurement residual-based approach to parameter error identification [45] and to an offline multiple-state-and-parameter estimation via an augmented state vector [46].

Previous work in PE has been confined to transmission systems, where higher measurement redundancy is typical and a reduced-order single-phase model is used [24]. This report outlines a process that includes full three-phase unbalanced DSSE and tracking of calculated parameter values over time in order to identify changes in parameter values. While DSSE has been explored extensively in recent years, PE techniques have so far not been applied to distribution systems. The application of PE techniques to distribution systems and microgrids could provide a new avenue for asset health monitoring and lead to reduced customer outage time and a more reliable system by enabling proactive maintenance and repairs.

For the analysis in the report, a combination of SCADA and AMI measurements is used as the data set, and both state vector augmentation and measurement residual-based approaches for the calculation of parameter values are adopted. The performance of the two PE techniques is compared.

A flowchart of the parameter diagnostics process is shown in Figure 17. The specific equations and algorithms for each block of the chart can be found in Section 3.3 and Section 3.4.

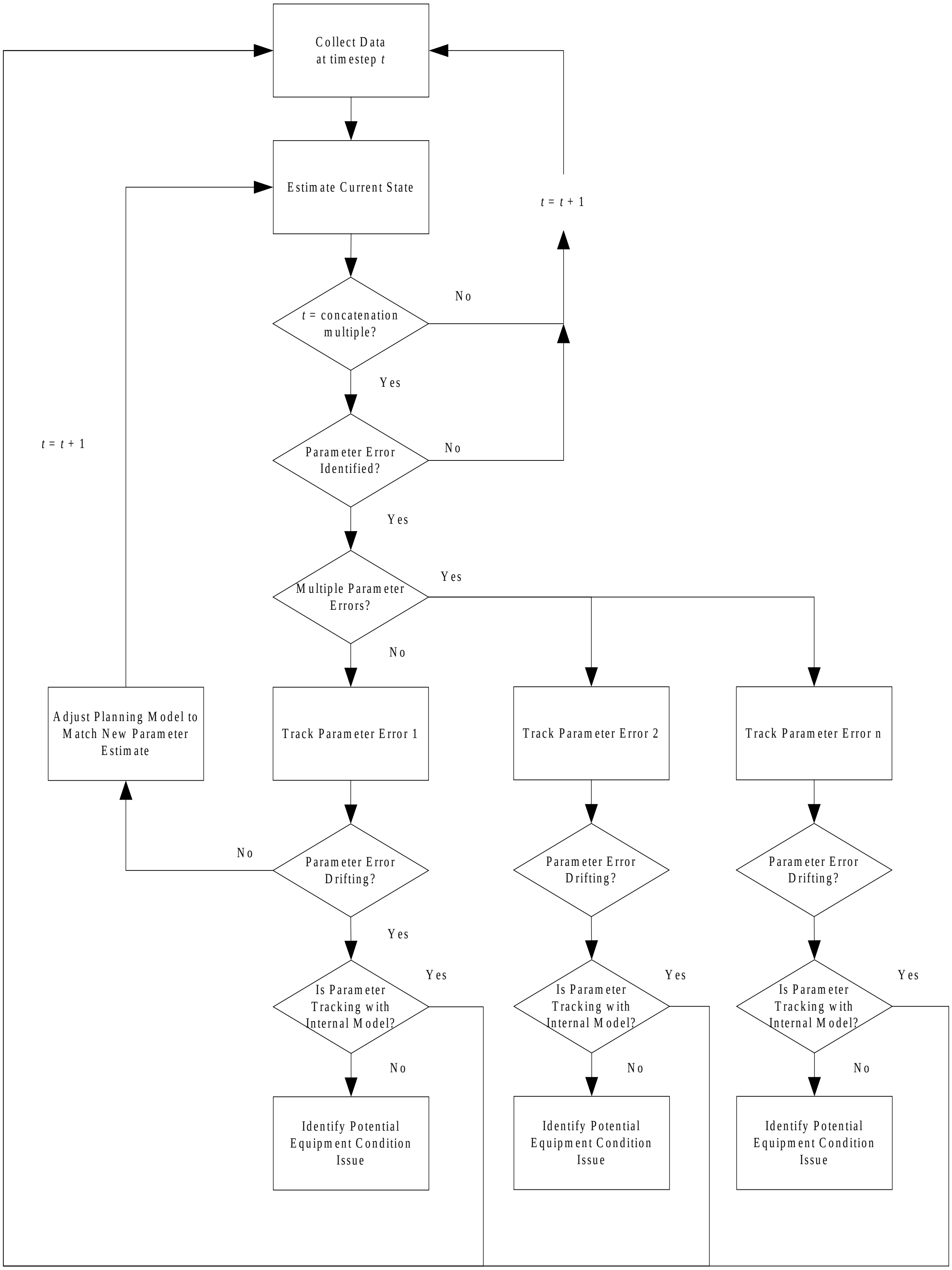
Collect Data at timestep t
Estimate Current State
t = t + 1
t = concatenation multiple?
No
Yes
t = t + 1
Parameter Error Identified?
No
Yes
Multiple Parameter Errors?
Yes
No
Adjust Planning Model to Match New Parameter Estimate
Track Parameter Error 1
Track Parameter Error 2
Track Parameter Error n
No
Parameter Error Drifting?
Parameter Error Drifting?
Parameter Error Drifting?
Yes
Yes
Yes
Yes
Is Parameter Tracking with Internal Model?
Is Parameter Tracking with Internal Model?
Is Parameter Tracking with Internal Model?
No
No
No
Identify Potential Equipment Condition Issue
Identify Potential Equipment Condition Issue
Identify Potential Equipment Condition Issue

Figure 17. Flow chart of evaluation methodology.

3.2 Data and Measurements in Distribution Systems

In this section, the types and locations of measurements that are available in distribution systems are discussed and the implications of using measurements recorded by AMI are explored.

In transmission systems, measurement devices transmit data in near real-time to a centralized Energy Management System (EMS), enabling an on-line SE process. At the transmission level there are enough measurements that the global redundancy, or ratio of total measurements to state variables, is over 4.0 [48]. In contrast, distribution systems have historically had few SCADA measurements outside of the substation, and even in modern systems where AMI data are available, redundancies are typically between 1.0 and 1.5 [49].

Typical North American distribution systems have untransposed conductors and unbalanced loading, so it is necessary for the system model to use a three-phase representation. The primary distribution system consists of a three-phase primary main feeder and laterals, with line-to-line voltage typically between 12.47kV and 34.5kV, as well as voltage control devices, shunt capacitor banks, and switches and other automation devices [50].

Measurements at the primary level include:

- Measurements at the substation typically include line current and bus voltage, all per-phase. From the line current and bus voltage, the power flow into the feeder is calculated. This data is collected by the SCADA system at intervals of 1s – 60s.

- Voltage control devices at intermediate primary system points, such as voltage regulators and shunt capacitor banks, may make measurements such as line current and voltage at the point of connection. These can be collected by the SCADA system at intervals of 1s – 60s.

- Utilities that have deployed feeder automation devices, such as remotely-operated switches and reclosers, may also measure the current and voltage on the primary system at the point of connection.

- Distributed generation is increasing rapidly and for some MW-scale systems, the energy production and system properties such as voltage at the interconnection point will be monitored and collected by the SCADA system.

- For residential customers, a single-phase, center-tapped service transformer is used to lower the voltage to the secondary system level and a triplex cable delivers power to the point of service at ±120V. For large commercial and industrial customers, a three-phase service transformer and quadruplex cable are typically used. No measurements are taken at the primary side of the typical service transformer. Figure 18 shows the components of a typical residential secondary system.

The AMI system supplies measurements recorded in the secondary system at the point of interconnection. Utilities may record only active energy consumption data, integrated over 5-60 minutes, for revenue metering purposes, or they may also choose to measure and record the reactive power consumption and/or voltage magnitude. Voltage magnitude measurements might be an average value over the integration window, or an instantaneous voltage measurement taken at a random time. Data are typically not transmitted to a central Meter Data Management (MDM) system in real-time, but collected in bursts at intervals of a few hours to 1 day, with transmission rates as low as 15 minutes in some cases [49].

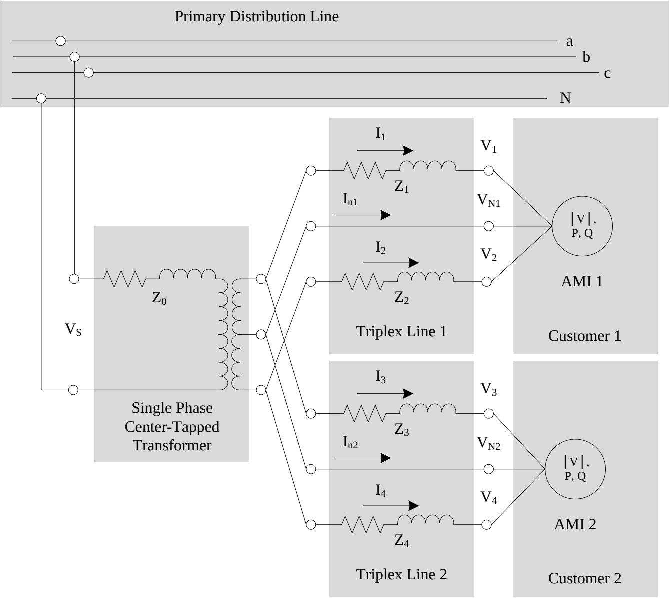
Primary Distribution Line
a
b
c
N
I_1
V_1
Z_1
I_{n1}
V_{N1}
I_2
V_2
Z_2
$|V|$,
P, Q
AMI 1
Triplex Line 1
Customer 1
Z_0
V_S
Single Phase
Center-Tapped
Transformer
I_3
V_3
Z_3
I_{n2}
V_{N2}
$|V|$,
P, Q
I_4
V_4
Z_4
AMI 2
Triplex Line 2
Customer 2

Figure 18. Principle components of a typical residential service system.

Load data are required for observability in DSSE, but AMI measurements are not typically available in real-time. Because of the lack of real-time load information, past approaches to on-line DSSE typically used pseudomeasurements. [31], [49]. Pseudomeasurements are estimated load shapes based on historical consumption or load allocation based on equipment ratings [28], [51]–[53]. The use of pseudomeasurements instead of actual AMI measurements results in a lower quality measurement set. The process proposed here for parameter tracking is an off-line process, not carried out in real-time, so can wait for actual AMI measurements as they are transmitted to the MDM to assemble a complete data set.

3.3 Distribution System State Estimation

This section outlines the method of DSSE and presents DSEE performance results from simulation studies.

3.3.1 Weighted Least Squares Formulation for Distribution System State Estimation

The WLS formulation of state estimation has been used extensively for transmission-level analysis and forms the basis for the proposed AMI-based DSSE method [54]. This section will examine the traditional balanced formulation, the unbalanced formulation, the inclusion of triplex secondary systems, and observability and redundancy issues.

3.3.1.1 Balanced Weighted Least Squares Formulation

The Normal Equations approach uses the WLS method to minimize the objective function *J(x)*.

$$J(x) = \sum_{i=1}^{m} \frac{(z_i - h_i(x))^2}{R_{ii}} \tag{22}$$

where:

m: number of measurements
z: vector of measurements
x: system state vector of complex voltage at each bus
$h(x)$: vector of nonlinear functions relating measurements to states
R: diagonal matrix of measurement variances

To minimize *J(x)*, the first order optimality condition must be satisfied:

$$g(x) = \frac{\partial J(x)}{\partial x} = -H^T(x)R^{-1}\left[z - h(x)\right] = 0 \tag{23}$$

where:

$H(x)$: Jacobian with respect to elements of the state vector

Due to the nonlinearity of the system, an iterative approach must be taken. Expanding *g(x)* into its Taylor Series centered about the state vector *x*, with the higher order terms ignored, the *(k+1)* iteration of the state vector is given below.

$$x^{k+1} = x^k - \left[G\left(x^k\right)\right]^{-1} \cdot g\left(x\right) \tag{24}$$

where:

x^k : is the state vector at iteration *k*
$G(x^k)$: the gain matrix at iteration *k*

The gain matrix, $G(x^k)$, is computed.

$$G\left(x^k\right) = \frac{\partial g(x^k)}{\partial x} = H^T(x^k)R^{-1}\left[H(x^k)\right] \tag{25}$$

Substituting (25) into (24) gives the final iterative form.

$$x^{k+1} = x^k - \left[G\left(x^k\right)\right]^{-1} \cdot \left(-H^T(x)R^{-1}\left[z - h(x)\right]\right) \tag{26}$$

A standard assumption in the balanced WLS formulation is that there is line transposition and balanced loading of the end-use loads [25]. These two assumptions allow for a single-phase representation of a transposed three-phase line segment as shown in Figure 19

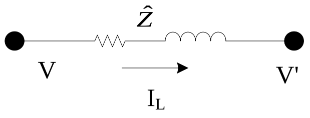

Figure 19. Three-wire ungrounded delta line segment in single-phase approximation.

With a single-phase representation of the line segments, the voltage drop is given by.

$$V = V' - \left(\hat{Z}\right) \cdot I_L \tag{27}$$

where:

V: voltage on the sending node
V': voltage on the receiving node
$\hat{Z}$: impedance of the line segment
I_L: current of the line segment

The active power injection at a node can be represented as shown below, with single values for the real and imaginary parts of the nodal admittance matrix, G_{mn} and B_{mn}.

$$P_m = V_m \sum_{n=1}^{N} V_n \left[G_{mn} \cos(\theta_{mn}) + B_{mn} \sin(\theta_{mn}) \right] \tag{28}$$

where:

P_m: three-phase power injection at node m
V_m: voltage magnitude at node m
N: number of nodes in the system
V_n: voltage magnitude at node n
G_{mn}: real part of nodal admittance matrix, Y
B_{mn}: imaginary part of nodal admittance matrix, Y
θ_{mn}: the difference in voltage angle at bus m and voltage angle at bus n

Equation (28) shows an example of a generalized $h(x)$ entry for the active power injection at node m. The vector of nonlinear functions relating measurements to state variables, $h(x)$, can include functions for nodal injections, line power flows, line currents, and voltages. This approach has been successfully used for several decades for analysis of the transmission system where power flows and voltage are assumed to be balanced. While appropriate at the transmission level, this assumption it is not effective for the majority of distribution systems in North America where feeders can be highly unbalanced and single- and double-phase laterals are used extensively.

3.3.1.2 Unbalanced Weighted Least Squares Formulation

DSSE, as outlined in [27], expands the standard Normal Equations, of which (28) is an example, to a three-phase implementation. For a full three-phase unbalanced state estimation, allowing for unbalanced flows and electromagnetic coupling between phases, the difference is in the formulations of $h(x)$ and $H(x)$. The size of the equation set is determined not by the number of nodes, but by the number of conductors [55]. Figure 20 shows a representation of a typical four-wire grounded wye line segment, which is the most common distribution feeder arrangement in North America. Because of the need to account for unbalanced loads and electromagnetic couplings, it is not accurate to use the single line representation as shown in Figure 20.

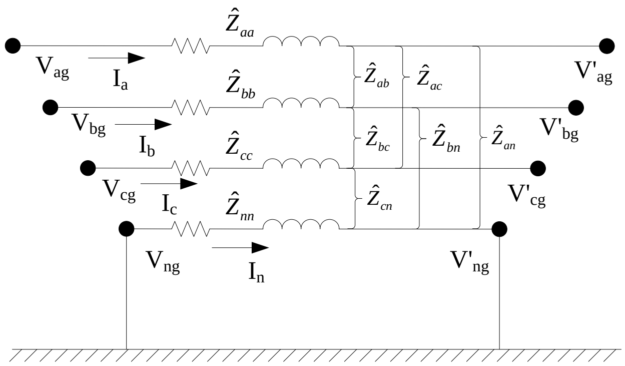

Figure 20. Four-wire grounded wye line segment.

Because of the lack of conductor transposition at the distribution level, and the unbalanced loading, the impedance of a line segment cannot be accurately represented by a single impedance value, $\hat{z}$; instead it requires a full-phase representation. The values of the primitive impedance matrix are calculated from the physical properties of conductors and their positions with respect to one another using a reduced form of Carson's Equations [56].

$$\begin{bmatrix} V_{ag} \\ V_{bg} \\ V_{cg} \\ V_{ng} \end{bmatrix} = \begin{bmatrix} V_{ag}^{'} \\ V_{bg}^{'} \\ V_{cg}^{'} \\ V_{ng}^{'} \end{bmatrix} + \begin{bmatrix} \hat{Z}_{aa} & \hat{Z}_{ab} & \hat{Z}_{ac} & \hat{Z}_{an} \\ \hat{Z}_{ba} & \hat{Z}_{bb} & \hat{Z}_{bc} & \hat{Z}_{bn} \\ \hat{Z}_{ca} & \hat{Z}_{ca} & \hat{Z}_{cc} & \hat{Z}_{cn} \\ \hat{Z}_{na} & \hat{Z}_{nb} & \hat{Z}_{nc} & \hat{Z}_{nn} \end{bmatrix} \cdot \begin{bmatrix} I_a \\ I_b \\ I_c \\ I_n \end{bmatrix} \tag{29}$$

In North America, it is common to assume that the neutral conductor is connected to earth ground through a zero ohm impedance at both ends. This grounding assumption allows for a Kron reduction of the primitive impedance matrix that results in a 3X3 phase impedance matrix [56]. Because of the structure of (29), it is not possible to use the formulation of the Normal Equations as shown in (28) as the basis for the *h(x)*. Instead, (28) is replaced by a set of power injection equations, one for each individual phase, with terms due to electromagnetic coupling of impedances as shown below.

$$\begin{aligned} P_m^a &= V_m^a \sum_{t \in p} \sum_{n=1}^{N} V_n^t \left[G_{mn}^t \cos(\theta_{mn}^t) + B_{mn}^t \sin(\theta_{mn}^t) \right] \\ P_m^b &= V_m^b \sum_{t \in p} \sum_{n=1}^{N} V_n^t \left[G_{mn}^t \cos(\theta_{mn}^t) + B_{mn}^t \sin(\theta_{mn}^t) \right] \\ P_m^c &= V_m^c \sum_{t \in p} \sum_{n=1}^{N} V_n^t \left[G_{mn}^t \cos(\theta_{mn}^t) + B_{mn}^t \sin(\theta_{mn}^t) \right] \end{aligned} \tag{30}$$

where:

$P^b{}_m$: power injection at node m, at phase b
$V^b{}_m$: voltage magnitude at node *m*, at phase *b*
p: subset of phases {*a*,*b*,*c*}
$V^b{}_n$: voltage magnitude at node *n*, at phase *b*
$G^t{}_{mn}$: real part of nodal admittance matrix, *Y*, at phase *t*
$B^t{}_{mn}$: imaginary part of nodal admittance matrix, *Y*, at phase *t*
$\theta^t{}_{mn}$: the difference in voltage angle at bus *m* and voltage angle at bus *n*, at phase *t*

The equations of (30) assume that the phasing of the line segment is the same at both ends, but it can be extended to include phase changes in the segment [55]. It can be seen that for a three-phase node it is necessary to formulate a separate active power injection equation for each of the phases. Using a formulation similar to the equations shown for active power injections, the other equations of *h(x)* can also be developed for the primary distribution system [27]. The formulation of (29) and (30) allow state estimation to be formulated for a fully unbalanced distribution system similar to what is used in parts of Europe. But to apply (29) and (30) to a North American type systems it is necessary to include the secondary distribution systems.

3.3.1.3 Inclusion of Triplex Secondary Systems

As discussed in Section 3.2, in North America, the typical residential secondary distribution system consists of a step-down transformer and service cable to the site of the customer meter. Similar to (29), it is possible to construct the primitive impedance matrices for the elements of the secondary distribution system. For a residential secondary system, the primitive impedance matrices are 3X3 matrices and can be reduced to 2X2 phase matrices assuming zero ohm impedance grounding to earth. The voltage drop across the transformer and triplex line, as was shown in Figure 18, is given below

$$\begin{bmatrix} V_1 \\ V_2 \end{bmatrix} = \begin{bmatrix} \frac{1}{n_t} & 0 \\ 0 & \frac{1}{n_t} \end{bmatrix} \cdot \left(\begin{bmatrix} V_S \\ V_S \end{bmatrix} - \begin{bmatrix} \left(Z_1 + \frac{1}{n_t^2}.Z_0 \right) & -\frac{1}{n_t^2}.Z_0 \\ \frac{1}{n_t^2}.Z_0 & -\left(Z_1 + \frac{1}{n_t^2}.Z_0 \right) \end{bmatrix} \begin{bmatrix} I_1 \\ I_2 \end{bmatrix} \right) \tag{31}$$

where:

n_t: high-side rated voltage/low-side half winding rated voltage

Equation (31) can be used as the basis to form the Normal Equations for the secondary distribution systems in the same manner.

3.3.1.4 Structure of Normal Equations and Jacobian

By using the Normal Equations for the primary and secondary distribution systems, it is possible to construct a complete WLS formation for an unbalanced, North American distribution system. This formulation allows for single-phase laterals and radial triplex secondaries. The elements of *h(x)* are similar to the traditional formulation except that there are additional sets of equations to account for the secondary distribution systems. For the presented work, the Normal Equations can include P_i, Q_i, and $|V_i|$ for the primary and secondary nodes. Power flows, P_{ij} and Q_{ij}, and current values, I_{ij}, are also included in *h(x*.

With the exception of the swing node, all primary node injections are virtual measurements: measurements of zero power injection that enforce energy conservation. The information that no power can be entering or leaving the node is known due to the topology, and that information is represented in the form of a measurement of zero power injection. These virtual measurements are necessary to create a complete measurement set that has observability at all points. The swing node is also the only primary node that has a voltage magnitude measurement. Similarly, with the exception of AMI meters, all secondary node injections are virtual measurements with a value of zero. AMI meters are also the only locations on the secondary distribution systems that have voltage magnitude measurements. Equation (32) shows the general structure of *h(x)*, divided by primary and secondary measurement sets.

$$h(x)=\begin{bmatrix}\text{primary}\\ \cdots \\ \text{secondary}\end{bmatrix}=\begin{bmatrix}P_i\\ Q_i\\ |V_i|\\ \cdots \\ P_i\\ Q_i\\ |V_i|\end{bmatrix} \tag{32}$$

The structure of the Jacobian, *H(x)*, follows the traditional formulation, with the rows representing the equations of the *h(x)* vector and the columns representing the state variables. The individual entries are the partial derivatives of the Normal Equations with respect to the state variables. The Jacobian will therefore be significantly larger than a single-phase formulation because of the increased number of equations in *h(x)*, the additional state variables associated with the secondary nodes, and the representation of equations by phase instead of by node.

3.3.1.5 Unbalanced Secondary Loading

The typical residential service in North America is a split-phase three wire service as shown in Figure 18. While Figure 18 shows three separate voltages at the AMI meter (V_1, V_2, and V_N), the current generation of AMI meters are only built to measure the difference between V_1 and V_2; active and reactive power measurements also are only single values. Because there is only a single set of measurements it is not possible to directly measure imbalances in the secondary system voltages; which introduces a small amount of error. Error is produced by the non-linear I^2R losses, and associated voltage drop, of the triplex line when current I_1 and I_2 are not equal. 120V loads such as lighting and plug loads are supplied by connecting between either V_1 or V_2 and V_N. 240V loads such as water heaters, electric ranges, and air conditioners are connected between V_1 and V_2.

3.3.2 Simulation Studies

To evaluate the AMI-based state estimation processes presented in the previous sections, modified versions of the IEEE 13 and 8500 Node Test Systems will be used [56]. The 13 Node Test System was modified to include the addition of radial secondary distribution systems as shown in Figure 18. The 8500 Node Test Feeder model includes the secondary system; balanced loads were used. Simulation of the modified IEEE 13 and 8500 Node Test Systems were conducted in the GridLAB-D simulation environment [4], [57]. The solutions of these simulations were then used to create error-free measurement sets, *z*, of real power injection, P_i, reactive power injection, Q_i, and voltage magnitude, $|V_i|$. Time-series loadshapes were created for residential and commercial customers. Residential customers were modeled with physics-based end-use loads in their homes, including HVACs, water heaters, and scheduled lighting and plug loads. GridLAB-D was also configured to output the network impedance and topology data necessary for the state and parameter estimation algorithms.

Measurement and parameter error were then added to construct the input measurement set, *z*, for the state estimator. As is typical in SE literature, measurements errors are assumed to be Gaussian with zero mean. This assumption is required for the application of SE algorithms. Measurements errors that have a non-zero mean would result in a systematic bias in SE results. Gaussian measurement error of up to 2.5% and parameter errors of up to 10.0% were considered. Gaussian error in parameter values was applied to all overhead and underground elements, including the single-phase center-tapped transformers and triplex lines. These values include the series and shunt resistances, shunt capacitances, line lengths, and the distances associated with conductor configurations.

The following sub-sections will examine various analysis cases to explore the performance of the proposed DSSE. The first case will examine the impact of various measurement and parameter errors on the IEEE 13 Node Test System. The second case will examine the impact of different AMI sample times and the third case will examine the impact of increasing the number of radial triplex lines from one to five per transformer. Case four will add a limited number of SCADA measurements and case five will add unmetered loads to the system. The sixth case will examine the estimators' performance on the larger IEEE 8500 Node Test System. These cases demonstrate the function of the unbalanced DSSE in a distribution, showing how the process is robust under realistic conditions and could be used to improve the operational knowledge of the state of a system, leading to more reliable operations.

3.3.2.1 Case 1: Base Case Results

The state estimation algorithm was applied to a modified version of the IEEE 13 Node Test System [56]. The lumped loads of the IEEE 13 Node Test System were replaced with triplex loads connected via secondary network models as shown in Figure 21. A standard single-phase center-tapped transformer model was used for all secondary transformers, as was a 1/0 triplex cable model, though the length of the lines varied [50].

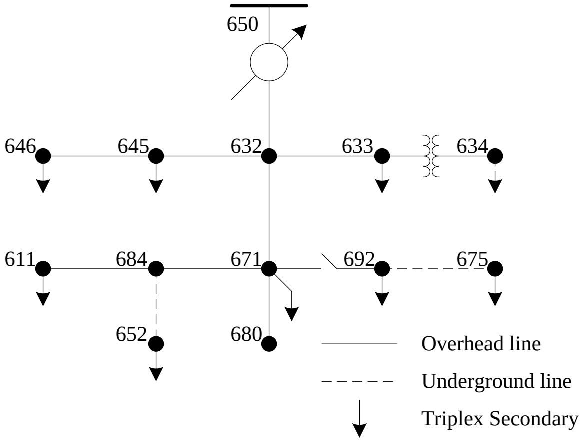

Figure 21. Modified IEEE 13 Node Test System.

The performance of the AMI-based state estimator is quantified by calculating the absolute value of the average difference between the true and estimated voltage magnitudes. While the difference in voltage angles could also be examined, angle variations at the distribution level are relatively small. Additionally, magnitudes are the values of interest for standards such as ANSI C84.1 [33]. $|V_{err}|$ is calculated as shown below.

$$\left|V_{err}\right| = \frac{1}{N}\sum\left|V_{true} - V_{estimated}\right| \tag{33}$$

Values of $|V_{err}|$, expressed as a percentage, are shown in Table 4 for various combinations of measurement and parameter error, also given as percent values.

Table 4. 13 Node Test System $|V_{err}|$ Values in Percent

		Parameter Error				
Measurement Error		0.0	1.0	2.5	5.0	10.0
	0.00	0.0001	0.0199	0.0504	0.1032	0.2140
	0.25	0.0786	0.0867	0.1044	0.1405	0.2356
	0.50	0.1571	0.1632	0.1788	0.2090	0.2845
	1.00	0.3143	0.3193	0.3310	0.3574	0.4182
	2.50	0.7863	0.7910	0.7984	0.8147	0.8643

When there is no measurement error, and perfect knowledge of the system parameters, the state estimation converges to a value of $|V_{err}|$ on the order 1e-7. This value is consistent with the convergence criteria of the power flow solution used to generate the measurement data. It can be seen that the values of $|V_{err}|$ increase monotonically as the measurement and parameter errors increase, with a value of 0.8643% when there is 2.5% measurement error and 10.0% parameter error. In operational systems, it is possible that errors in parameter values stored in the system model might be even larger, especially in the secondary system. For example, it is rare for the true length of the triplex cables to be recorded.

For the values shown in Table 4, it was assumed that all measurements are instantaneous values. This was done to show the performance of the state estimation process, but it is not an accurate representation of how AMI values are collected by smart meters.

3.3.2.2 Case 2: Variable AMI Measurement Times

AMI systems provide power measurements in the form of averaged energy values and a voltage value that is an average over a given period of time; commonly 5 minutes, 15 minutes, 30 minutes, or 60 minutes. In order to isolate the effect of different AMI sample times Case 2 will examine a system with no measurement or parameter error. Figure 22 shows the value of $|V_{err}|$ as the AMI sample time is increased from 1 minute to 60 minutes. For this case, $|V_{err}|$ is the difference between the estimated voltage and the actual real time value of voltage; something which is not measured directly by the AMI meter.

Figure 22. Plot of $|V_{err}|$ vs. AMI sample time.

From Figure 22 it can be seen that as the AMI sample time is increased it introduces an increasing amount of error into the estimated value of the state variables, as quantified by $|V_{err}|$. But even with a sample time of 60 minutes the introduced error is less than 0.15%. This is due in part to the fact that over the 1-hour period the average voltage at the AMI meters only changed by 0.26%, due in part to the active voltage control of the substation regulator, and in part to the fact that the 13 Node Test System is an electrically “stiff” system.

3.3.2.3 Case 3: Increased Number of AMI Meters per Transformer

In Case 1 and 2 it was assumed that the customer meters were supplied by service transformers that had only one triplex line each. In practice, it is common for a single service transformer to supply multiple loads each through their own triplex line. In order to isolate the effect of having additional measurement values, Case 3 will examine a system with no measurement or parameter error, and instantaneous AMI measurements. Case 3 will examine the value of $|V_{err}|$ as the number of triplex lines per service transformer is increased from one to five. As the number of triplex lines is increased the number of state variable will also increase because of the additional nodes in the system; each triplex line will add two additional state variables.

Figure 23 shows that the value of $|V_{err}|$ decreases slightly as the number of lines is increased from one to five. For the results from the modified 13 Node Test System shown in Figure 23, the global redundancy increased from a value of 1.17 with a single triplex line, to a value of 1.33 when there are five triplex lines. While there are not always multiple triplex lines per transformers, it is important to note that the addition of these lines affects redundancy.

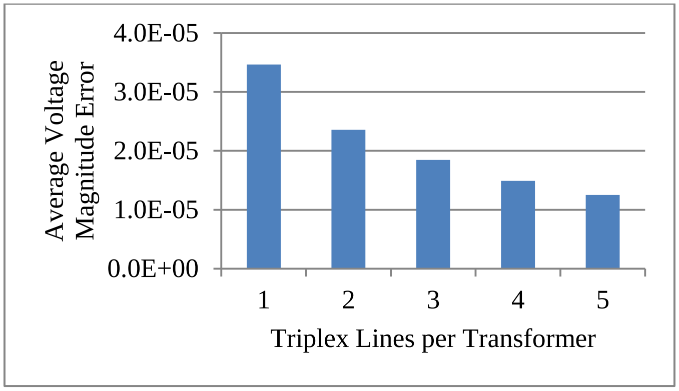

Figure 23. Plot of $|V_{err}|$ vs. number of AMI meters per secondary transformer.

3.3.2.4 Case 4: Addition of Limited SCADA Measurements

In the previous sub-sections, it was assumed that with the exception of the substation measurements there were no SCADA measurements available. This sub-section will examine the improved performance if SCADA values from the primary distribution system are added to the case presented in Table 4. Table 5 shows the values of $|V_{err}|$ that are obtained with the inclusion of addition SCADA measurements. For the 13 Node Test System voltage magnitudes were added at nodes 611 and 675. These nodes were selected because there are capacitors connected here and it is not uncommon to have capacitors connected to a utility’s SCADA system. Node 611 is a single voltage measurement on phase *c* and node 675 has measurements on each of the three phases.

Table 5. 13 Node Test System $|V_{err}|$ Values with Limited SCADA Measurements

		Parameter Error				
		0.0	1.0	2.5	5.0	10.0
Measurement Error	0.00	0.0001	0.0199	0.0503	0.1030	0.2136
	0.25	0.0788	0.0861	0.1036	0.1395	0.2342
	0.50	0.1576	0.1626	0.1775	0.2073	0.2827
	1.00	0.3152	0.3191	0.3296	0.3548	0.4150
	2.50	0.7886	0.7920	0.7981	0.8127	0.8586

By comparing in Table 5 to Table 4 it can be seen that the inclusion of voltage magnitude measurements on the primary distribution system provide a slight improvement to the accuracy of the estimate. It is also possible to adjust the weighting of measurements in the R matrix to further reduce the values of $|V_{err}|$ but for the purposes of comparison, the same values were used for the R matrix in Table 4 and Table 5.

3.3.2.5 Case 5: Unmetered Load

Not all loads on a distribution system are metered; municipal loads such as street lighting and traffic signals may intentionally be unmetered. In addition to the intentionally unmetered load, some systems have to contend with power theft. Case 5 will examine the ability of the proposed DSSE to perform in the presence of loads that are not metered as part of the AMI system. For Case 5 an unmetered load is added to phase *b* of node 680 and is supplied by the existing phase *b* service transformer. The information associated with this unmetered load is not available to the state estimator, and decreases the accuracy of the estimate as the load increases. Figure 24 shows the increasing value of $|V_{err}|$ as the magnitude of the unmetered load is increased from zero to approximately 5% of the total feeder load. From Figure 24 it can be seen that the AMI-based DSSE is able to accurately estimate the state values even when there is a significant amount of unmetered load.

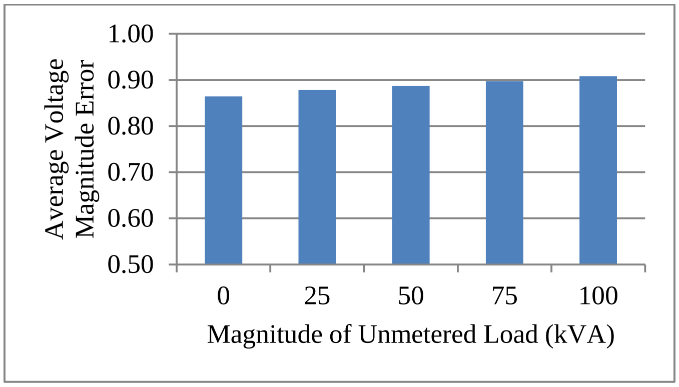

Figure 24. Plot of $|V_{err}|$ as the unmetered load on phase *b* is increased.

3.3.3 Case 6: IEEE 8500 Node Test System

The previous sub-sections showed the effectiveness of the proposed methods on a small test system. This sub-section examines its performance on a modified version of the larger IEEE 8500 Node Test System, as shown in Figure 25 [58]This system also includes triplex secondaries servicing end-use customers. The length of the triplex conductor was randomly varied. The purpose of this is to show that the method is extensible to larger systems.

Case 6 assumes 2.5% measurement error, 10.0% parameter errors, a 15-minute sample time for AMI meters, and only a single triplex line per secondary service transformer. No SCADA values other than the substation values are included. Additionally, a number of unmetered loads have been added throughout the system that system that represent approximately 5% of the total feeder load. With these values, the state estimator converged to a $|V_{err}|$ value of 1.1771%. This clearly shows that the proposed DSSE method is able to operate effectively under realistic operational conditions. The average value of 1.1771% is much lower than the average measurement error of 2.50%.

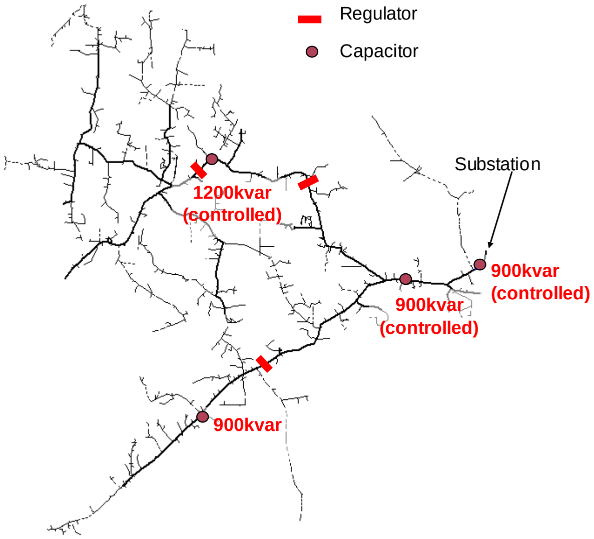

Figure 25. IEEE 8500 Node Test System. Fig reproduced from [58].

This section has presented a WLS DSSE that uses AMI measurements as the primary data source. It has been shown that the presented method is able to account for the unbalanced load, and topologies, of distribution systems in North America. Simulations run on standard IEEE test systems have shown that it is able to accurately estimate the state variables in the presence of significant measurement and parameter error, as well as errors introduced by AMI sample times and unmetered loads. While the requirements to implement the proposed system do not currently exist at many utilities, the industry trend is to increasingly integrate AMI data into real-time control systems, facilitating the use of the proposed DSSE methodology. The DSSE process demonstrated here under realistic conditions increases the situational awareness of grid operators, allowing better decisions and more reliable and resilient service.

3.4 Distribution System Parameter Estimation

This section outlines the method of distribution system PE and presents performance results from simulation studies. Distribution system PE could be used to track changing parameter values over time in order to detect signs of degradation that might indicate that preventative maintenance or replacement is warranted. Such a parameter tracking system would lead to reduced customer outage time and a more reliable system. Here, we focus on series impedance parameters. A change in series impedance parameter could be brought about by, for example, an imminent failure of a cable splice, breaker contact degradation, or transformer shorting. All of these equipment failure mechanisms may be foreseen by a process that can track series impedance parameter values over time, which could result in reduced customer outage time and increased reliability.

3.4.1 Methods

Two different PE methods are considered: residual sensitivity analysis (referred to as RA in discussion) and state vector augmentation using Kalman Filter (referred to as KF in discussion). The technique of combining measurements from multiple measurement snapshots into a single PE is used to improve the robustness of the estimate.

3.4.1.1 Residual sensitivity analysis

PE based on residual sensitivity analysis performs an extra step after the SE process concludes to compute a residual sensitivity matrix S [24]. The sensitivity matrix gives the relationship between residuals and measurement errors,

$$r = Se \tag{34}$$

where:

r: measurement residuals
S: sensitivity matrix

A linear relationship can be found between measurement residuals and parameter error [41], [42].

$$r_s = \left(S_{ss} \frac{\partial h_s}{\partial p} \right) \varepsilon + \overline{r_s} \tag{35}$$

where:

$_{ss}$: refers to subset of related measurements
S_{ss}: sub-matrix of S corresponding to s measurements related to p
h_s: nonlinear functions relating measurements to states
$\overline{r_s}$: residual that would have been found with correct parameter
p: parameter
ε: error in parameter value

The relationship given in (35) can be interpreted as a local estimation problem and the optimal value of ε in the least squares sense can be computed [42]:

$$\varepsilon = \left[\frac{\partial h_s^T}{\partial p} R_s^{-1} S_{ss} \frac{\partial h_s}{\partial p} \right]^{-1} \frac{\partial h_s^T}{\partial p} R_s^{-1} r_s \tag{36}$$

where:

R: diagonal matrix of measurement uncertainties.

The measurement residuals are a byproduct of the SE process, but the calculation of S requires an additional post-SE step to calculate and involves inverting the Gain matrix [24]. Because the size of the Gain matrix scales with the size of the system and the size of measurements, the computation becomes more computationally taxing as system size increases. For a SE process that is operating in a “real-time” constraint, this may not finish processing the current SE before the new set of data arrives. Methods to improve the computational efficiency are needed to maintain these real time constraints. However, the time scales of this project and the off-line nature of the initial study do not have such constraints.

Methods to speed up the SE process have been well documented in transmission SE and are applicable here [59]. However, this work focuses on the mechanics and capabilities of the distribution SE process, with improved computational efficiency saved for future investigations.

3.4.1.2 State vector augmentation

The state-vector augmentation approach was originally proposed in [35]. The approach starts with an initial guess of the parameter values and iteratively improves the values by computing the gain matrix and updating the parameter covariance matrix using the measurements at different time steps during a period. The parameter values are assumed to be constant during the entire time period and are combined with the state vector to form an augmented state vector.

More precisely, a nonlinear dynamical system can be represented as

$$x_k = f(x_{k-1}, u_{k-1}, w_{k-1}) \tag{37}$$

$$z_k = h(x_k, v_k), \tag{38}$$

where the state vector x_k is a nonlinear function of the previous states x_{k-1}, the previous inputs/control u_{k-1}, and the process noise w_{k-1} (zero mean Gaussian). The measurements z_k are a nonlinear function of the current state and measurement noise v_k (also zero mean Gaussian). The state transitions can be computed in the same way as linear KF, except that the transition and observation matrices are replaced by the Jacobians of f and h. This modified version of KF is called the extended KF.

State augmentation modifies the state vector by concatenating the parameters of interest, i.e., $x \coloneqq [x_s, x_p]$, where x_s includes all the states and x_p includes all the parameters that need to be estimated. The prediction covariance matrix P is augmented to become a block diagonal matrix:

$$P \coloneqq \begin{bmatrix} P_s & 0 \\ 0 & P_p \end{bmatrix}. \tag{39}$$

At each time step, the measurement values are predicted using the estimated state and parameter values from the previous time step. The predicted values are compared with the actual measurements, and the difference is used to compute the gain matrix. The parameter covariance matrix is updated as a corresponding block of the inverse of the gain matrix. The new parameter covariance matrix is used to compute the gain matrix for the next time step. More details can be found in [24], [35].

3.4.1.3 Combining multiple measurement snapshots

For the estimation of parameter values that can be assumed to be constant (aside from diurnal temperature-related variations) over a period of months or years, such as series impedance values, improvements to the result can be obtained by combining the information in several measurement snapshots into a single estimate of a parameter value [24]. While diurnal variations can be significant in some climates, the effect can be minimized by combining the measurements from a whole number of days into a single parameter estimate, in order to look for longer-timescale variations in parameter values.

For the residual sensitivity PE method, given that the DSSE and PE procedure are executed sequentially, the PE can be extended to use the information from multiple measurement snapshots in a single PE. For example, to combine the *k* measurement snapshots for a single parameter value calculation, the outputs from the DSSE are combined as

$$r = \begin{bmatrix} r_1 \\ r_2 \\ \vdots \\ r_k \end{bmatrix}, \tag{40}$$

$$\partial h/\partial p = \begin{bmatrix} \partial h/\partial p_1 \\ \partial h/\partial p_2 \\ \vdots \\ \partial h/\partial p_k \end{bmatrix}, \tag{41}$$

and

$$S = \begin{bmatrix} S_1 & 0 & 0 & 0 \\ 0 & S_2 & 0 & 0 \\ 0 & 0 & \ddots & 0 \\ 0 & 0 & 0 & S_k \end{bmatrix}. \tag{42}$$

The size of each of the components in (40) increases linearly with the number of measurement snapshots that is to be combined. However, this does not require increasingly computationally complex matrix inversion in the parameter estimation calculation in (40), since the result of the multiplication of the elements inside the square bracket in (40) is a [1x1] and R is a diagonal matrix. While the computational complexity of the calculation of the S matrix scales with system size, the approach of combining results from multiple measurement scans into a single parameter estimation does not result in additional increasing computational complexity as system size increases.

For the Kalman Filter-based method, the state vector is extended to include all state variables from the timesteps that are combined, as well as the parameter to be estimated. Matrices used in the calculation such as *H*, *G*, etc., are combined as block diagonal matrices [24], with each block corresponding to one measurement snapshot.

3.4.2 Simulation Studies

The PE methods were tested on the same modified IEEE 13 Node Test Feeder described in Section 3.3.2.1. The GridLAB-D solution was used to create error-free measurement sets, $z(t)$, at 5-minute intervals:

- Power injection, P_{inj}, Q_{inj}, and $|V|$ at substation
- $P_{in}j$, Q_{inj}, and $|V|$ at non-triplex loads
- Power flow, P_{flow} and Q_{flow}, and $|V|$ at primary system nodes with voltage regulator or shunt capacitor bank
- $P_{in}j$, Q_{inj}, and $|V|$ at AMI meters
- Virtual measurements (constraints enforcing energy conservation) of $P_{inj}=0$ and $Q_{inj}=0$ at primary system nodes with no loads and no SCADA measurements

This measurement set does not include pseudomeasurements, or measurements that are constructed based on historical load shapes. With this measurement set, the redundancy of the system for SE was 1.30.

Measurement error was added to each measurement (except the virtual measurements). Measurement noise was assumed to follow a Gaussian random distribution with zero mean, and noise was uncorrelated from one measurement snapshot to the next [24]. The standard deviation of parameter error $\sigma(e_p)$, the gross error in each parameter that makes up the system model, is always assumed to be 10% in this study. In order to test the PE algorithms for the ability to detect change over time, a sudden change in the parameter value is introduced in the middle of the simulation. The parameter being estimated in this study was the resistance on phase a of a three-phase overhead cable connecting node 630 and node 632.The resistance of the cable on phase a is doubled, from 0.07Ω to 0.14Ω.

A sudden change to a series parameter value is used to demonstrate the process. Changes in series parameter values could be brought about by, for example, an imminent failure of a cable splice, breaker contact degradation, or transformer shorting. Changes in shunt parameter values could also be used to detect equipment failure, but because of the small magnitude of these values in distribution systems and microgrids, compared to typical measurement noise, they are not able to be addressed by this process.

For all the simulation cases, the number of total simulation steps is 576 (2 days of data given 5-minute measurement intervals). The mean and standard deviation of the PE errors over the entire simulation time are used as the metrics to evaluate the estimation performance. The mean of errors reflects the accuracy of the algorithms. Accurate estimates will have a mean close to 0, where the tolerance level is defined by the users. The standard deviation shows how uncertain the estimate is. A small standard deviation (compared to the actual parameter value) is desired in order to detect changes in the parameter value.

The two PE methods are first applied to measurement data, using a single measurement snapshot for each PE step. In Figure 26, the parameter error estimated by both methods is plotted with respect to time. The plot shows the estimated values one day before and after the sudden change. The standard deviation of measurement error, $\sigma(z_k)$, is assumed to be 0. It is shown that the residual analysis can detect the sudden change immediately when the measurement noise is 0. This is because the estimated parameter value at each time step is obtained independently from previous time steps by using the residuals of the current time step, while the KF-based method needs the measurements from a period of time to update the estimated values gradually and converge to a new value after the sudden change. As shown in in Figure 26, it took the KF about 8 hours after the sudden change to have similar performance as RA. However, the sudden change cannot be detected using RA when measurement noise is added.

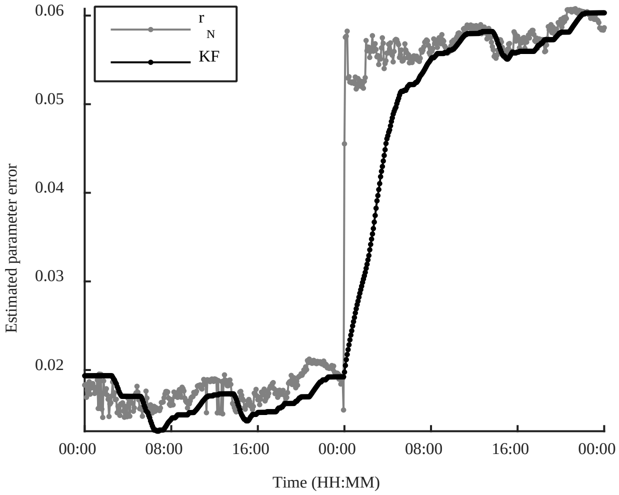

Figure 26. Estimated parameter error with no measurement noise and single snapshot using RA (in grey) and KF (in black)

Figure 27 shows the results for a scenario that is the same as in Figure 26, except that the measurement noise level $\sigma(z_k)$ is 1% instead of 0%. It can be seen that the PE result using residual analysis is significantly affected by the measurement noise. When the measurement noise level increases from 0% to 1%, the average estimated value deviates from the true value by 0.0119 and 0.0180 for RA and KF, respectively. However, the estimation results for RA oscillate within a large range around the true values with a standard deviation of 0.1262. Using state-vector augmentation, the difference between the estimates at different times is much smaller when measurement noise is present; the standard deviation of noise is only 0.0042.

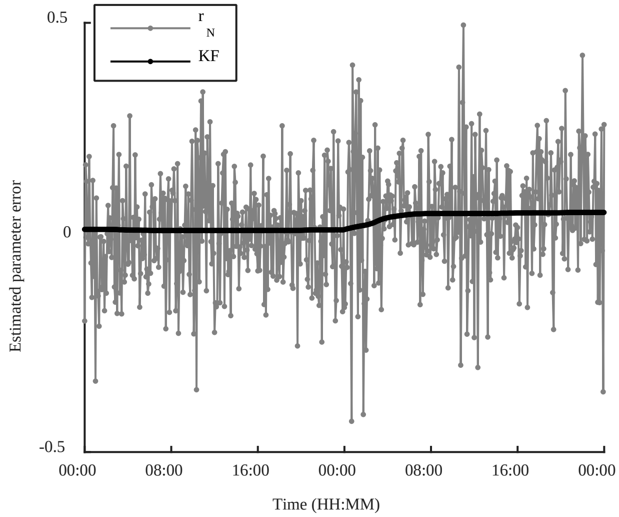

Figure 27. Estimated parameter error with 1% measurement noise and single snapshot using RA (in grey) and KF (in black)

The mean and the standard deviation of the estimated errors for the two cases are given in Table 6 and Table 7. For the single time step case, the number of combined snapshots t_c is 1. More cases with nonzero measurement noise are presented in the tables. The mean of the estimation errors is always relatively small (less than 0.02) for either method. The average error is always nonzero because the 10%

parameter error in all other system parameters may induce a persistent bias in the estimates. However, it can be noticed that the performance of the residual analysis based method becomes much worse as the amount of measurement noise increases. The standard deviation of the estimation errors is much larger than what is shown in Figure 26, hence the accuracy and the confidence in the estimated values will decrease. It is easy to see in Figure 27 that the RA estimation errors has a large range that deviates more than 0.2 away from the actual values, which is larger than the actual value after the sudden change. Therefore, it is not clear if a change in the parameter value has occurred and where it occurred. In addition, the estimated values will also be highly dependent on the number of time steps due to the large variation. In order to improve the RA results, multiple snapshots are necessary to increase the measurement redundancy. In contrast, the performance of KF is more stable because the changes in the mean and standard deviation of the errors are very small (less than 0.02 and 0.006, respectively) for different measurement noise levels. Therefore, the change in the parameter value can be clearly seen during the parameter tracking process.

Table 6. Mean of PE errors using RA and KF

$\sigma(z_k)$	$t_c = 1$		$t_c = 12$		$t_c = 24$	
	RA	KF	RA	KF	RA	KF
0.00%	0.0190	0.0178	0.0097	0.0094	0.0188	0.0188
0.50%	0.0174	0.0150	0.0091	0.0061	0.0180	0.0154
1.00%	0.0119	0.0180	0.0167	0.0190	0.0163	0.0192
1.50%	0.0026	0.0180	0.0048	0.0097	0.0138	0.0192

Table 7. Standard deviation of PE errors using RA and KF

$\sigma(z_k)$	$t_c = 1$		$t_c = 12$		$t_c = 24$	
	RA	KF	RA	KF	RA	KF
0.00%	0.0022	0.0043	0.0168	0.0174	0.0020	0.0041
0.50%	0.0626	0.0054	0.0259	0.0174	0.0132	0.0060
1.00%	0.1262	0.0042	0.0373	0.0039	0.0261	0.0035
1.50%	0.1922	0.0042	0.0595	0.0172	0.0393	0.0034

The two methods can be applied to measurement data using various numbers of consecutive measurement snapshots. The measurements from a number of multiple snapshots are combined to compute the parameter value at the end of the time window. Then the next set of measurements, following the already used measurements, is combined to continue similar process for estimating the parameter again. In this study, the number of multiple snapshots t_c is set to be 12 and 24, which includes data from a time window of 1 and 2 hours with 5-minute measurement intervals. The number of total time steps is still 576 (2 days), so that the number of the total sets of combined snapshots is 24 and 12, respectively.

In Figure 28, the PE errors are plotted for combining every hour's data (12 combined time steps) with measurement noise $\sigma(z_k) = 1\%$ and parameter error $\sigma(e_p) = 10\%$. By comparing to Figure 27, it shows that with more measurement noise, better performance can be obtained for both methods if multiple measurement snapshots are used. However, the results using RA still has much more variation than the KF results. It is still not clear to see where the sudden change occurred.

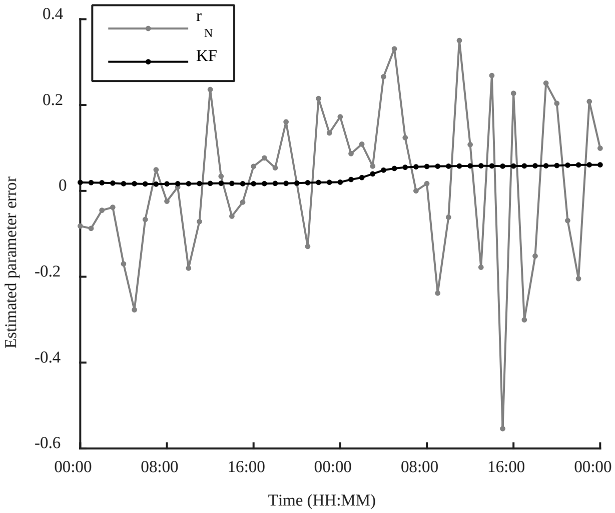

Figure 28. Estimated parameter error with 1% measurement noise and 12 combined time steps using RA (in grey) and KF approach (in black)

The mean and standard deviation of the PE errors for $t_c = 12$ and 24 are given in the remainder of Table 6 and Table 7. Similar to the results for using single time steps, Table 6 shows that the mean of the estimation errors is always relatively small in all the cases for both methods. For the residual analysis based method, it can be seen from Table 7 that the standard deviation of the errors decreases as the number of combined snapshots increases for all the cases that have nonzero measurement noise. However, when the measurement noise is relatively large, the standard deviations can be very large (e.g., more than half of the step change when $\sigma(z_k) = 1.5\%$), which will make the detection of the sudden change very difficult or even impossible. In all cases, the KF results are very stable with similar results for different measurement noise levels. It can also be noticed that the standard deviation of the KF results is not better when multiple snapshots are used. From the above results for both methods, it can be concluded that, in this simulated system, using multiple snapshots can improve the RA results, but the standard deviations of the errors are still too large to detect the sudden change. Using single snapshots is sufficient for the KF to give results showing a clear change in parameter value and it is not necessary to use multiple measurement snapshots. These two methods were also tested by estimating other parameters in the same system. The results are consistent with Table 6 and Table 7.

Overall, using state-vector augmentation with a Kalman filter can detect the designed sudden change in parameter value with measurement noise levels as large as 1.5% (or even larger). In addition, it did not require multiple measurement snapshots to improve estimation accuracy. The approach based on residual sensitivity analysis is not as robust as the KF approach. The estimates are very sensitive to measurement noise, and the performance became worse when the measurement noise level increased. Finding that the KF approach is better than RA is also consistent with statistical theory because the augmented model is more flexible, and will need to search a larger space of parameters than a two-step model.

3.5 Conclusions and Future Work

This project has developed an unbalanced DSSE and an off-line parameter tracking procedure for series impedance parameter values. An unbalanced DSSE is performed and then an estimate of the parameter value is carried out, optionally combining information from multiple measurement snapshots to increase local redundancy and the robustness of the estimate. While the simulated results of the PE method are promising, there are limitations to the parameters that are able to be addressed. Series parameters can be accurately assessed by these methods, but shunt parameters are not able to be estimated under realistic assumptions of measurement redundancy and measurement noise. In future, it is possible that the addition of new measurement techniques, such as microPMUs, to distribution systems will enable the estimation of a wider array of parameter values.

The widespread deployment of sensors at the distribution level is enabling observability into the distribution system. This observability enables the tracking of the state of distribution system and microgrid equipment over time. A system can be developed using the AMI data that is transmitted to the utility to carry out SE and PE of system model parameters, such as the resistance of cables and connections. These tracked equipment parameters could then be integrated into a larger asset management system that will allow utilities to determine when proactive replacement of equipment is warranted. This system would increase the system reliability and resiliency by reducing unplanned outages, and reduce costs by only replacing equipment when appropriate.

4.0 Conclusions

Many aspects of modern society rely heavily on electric power being readily and reliably available. During weather events and other outages on the system, this service is disrupted and can lead to financial losses, degradation in quality of life and health, and other societal impacts. Improving the overall resiliency in the distribution grid helps mitigate the large-scale impacts of such outages, as well as aid in the quicker restoration of the service.

The research presented in this report helps improve the resiliency of the distribution grid through two different approaches: microgrid operations, and distribution state and parameter estimation. Microgrid operations involve operating distributed resources in an islanded form to provide power to customers during a disruptive event. This can be as simple as a backup generator for a single building, or utilizing intact distribution system architecture to form a community microgrid or black start resource. Evaluating the unique constraints of the distribution system to ensure the microgrid can be formed, as well as any operational considerations, is needed to ensure power is available for the defined resources. The use of GridLAB-D’s simulation capability or operational nomograms helps provide emergency and distribution dispatchers the information they need to successfully execute the use of these microgrids to help improve the resiliency and restoration capability of distribution power systems.

The second approach, distribution-level state and parameter estimation, provides greater insight into the distribution system for more efficiency and resilient operations. Using distribution-level state estimation, states of operation and large measurement or model errors can be detected. When coupled with parameter estimation and long-term analysis, it can aid in spotting impending equipment failures, such as cable splice or transformer failures. Early detection of these conditions can allow their replacement or repair prior to a system outage, reducing outage times and improving the overall resiliency of the grid.

Once a disruptive event occurs, the two research topics can help maintain and restore service in a complementary, timely fashion. The reconfiguration algorithms and dynamic simulation capabilities provide operational procedures and nomograms for activating and utilizing the distributed assets in a meaningful manner. With the distribution state estimation active and underlying model updated to reflect the new microgrid state, errors in the measurements and model can be tracked. Under long enough operations, the parameter estimation aspect could aid in refining the model, as well as detecting impending failures in the microgrid.

Through the combined pre- and post-event techniques described, microgrids and distribution-level state and parameter estimation can greatly improve the resilience of the distribution system to major outages. In the event of a larger outage, the techniques and information from these two techniques can provide faster restoration of critical loads and services to the grid. Such improved resiliency and operations are critical for not only today’s power grid, but also for future applications like smart cities and completely islanded systems.

References

[1] "Consortium for Electric Reliability Technology Solutions (CERTS)." [Online]. Available: http://certs.lbl.gov. [Accessed: 21-Aug-2015].

[2] J. P. Lopes, C. Moreira, and A. Madureira, "Defining control strategies for MicroGrids islanded operation," *IEEE Trans. Power Syst.*, vol. 21, no. 2, pp. 916–924, 2006.

[3] F. Katiraei and M. Iravani, "Power Management Strategies for a Microgrid with Multiple Distributed Generation Units," *IEEE Trans. Power Syst.*, vol. 21, no. 4, pp. 1821–1831, 2006.

[4] "GridLAB-D." [Online]. Available: http://www.gridlabd.org/.

[5] K. Schneider, J. Fuller, F. Tuffner, D. Wu, M. Elizondo, M. Rice, A. Somani, A. Fisher, and B. Vyakaranam, "Modeling and Simulation Capabilities for the Evaluation of Micro Grids," Richland, WA, 2013.

[6] K. Schneider, F. Tuffner, and M. Elizondo, "Microgrids as a Resiliency Resource," Richland, WA, 2014.

[7] M. Elizondo, F. Tuffner, and K. Schneider, "Three-phase Unbalanced Transient Dynamics and Powerflow for Modeling Distribution Systems with Synchronous Machines," *IEEE Trans. Power Syst.*, vol. PP, no. 99, pp. 1–11, 2015.

[8] P. Garcia, J. L. Periera, S. C. Jr., V. da Costa, and N. Martins, "Three-phase Power Flow Calculations Using the Current Injection Method," *IEEE Trans. Power Syst.*, vol. 13, no. 2, pp. 508–514, 2000.

[9] P. W. Sauer and M. A. Pai, *Power System Dynamics and Stability*. Champaign, IL, USA: Stipes, 2006.

[10] R. C. Jaeger, *Microelectronic Circuit Design*. Boston, MA, USA: McGraw-Hill, 1997.

[11] T. H. Demiray, "Simulation of Power System Dynamics using Dynamic Phasor Models," Swiss Federal Institute of Technology Zurich, Zurich, Switzerland, 2008.

[12] P. Zhang, J. Marti, and H. Dommel, "Shifted Frequency Analysis for EMTP Simulation of Power System Dynamics," *IEEE Trans. Power Syst.*, vol. 57, no. 9, pp. 2564–2574, 2010.

[13] H. W. Dommel, "Transformer Models in the Simulation of Electromagnetic Transients," in *Proceedings of the 5th Power Systems Computing Conference*, 1975.

[14] "PSCAD Home." [Online]. Available: http://hvdc.ca/pscad. [Accessed: 21-Aug-2015].

[15] "Annual Energy Outlook 2013 with Projections to 2040," Washington D.C., 2013.

[16] "2010 Smart Grid System Report - Report to Congress," Washington D.C., 2012.

[17] A. W. B. Wollenberg., *Power Generation Operation and Control*. John Wiley & Sonns, Inc.

[18] "IEEE Guide for Investigating and Analyzing Power Cable, Joint, and Termination Failures on Systems Rated 5 kV Through 46 kV," *IEEE Std 1511-2004*. p. 0_1, 2004.

[19] W. L. Cooley, R. L. McConnell, and H. W. Hill Jr., "Use of Cable Surface Temperature to Detect High-Resistance Splices," *Industry Applications, IEEE Transactions on*, vol. IA-19, no. 3. pp. 434–439, 1983.

[20] N. T. Stringer and L. A. Kojovic, "Prevention of Underground Cable Splice Failures," *Industry Applications, IEEE Transactions on*, vol. 37, no. 1. pp. 230–239, 2001.

[21] F. C. Schweppe, "Power System Static-State Estimation, Part I: Exact Model," *IEEE Trans. Power Appar. Syst.*, no. 1, pp. 120–125, 1970.

[22] F. Schweppe and D. Rom, "Power System Static-State Estimation, Part II: Approximate Model," *IEEE Trans. Power Appar. Syst.*, vol. PAS-89, no. 1, pp. 125–130, Jan. 1970.

[23] F. Schweppe, "Power system static-state estimation, Part III: Implementation," *IEEE Trans. Power Appar. Syst.*, no. 1, pp. 130–135, 1970.

[24] A. Abur and A. Gomez Exposito, *Power System State Estimation: Theory and Implementation*. New York: CRC Press, 2004.

[25] K. A. Clements and A. Simoes Costa, "Topology Error Identification Using Normalized Lagrange Multipliers," *IEEE Trans. Power Syst.*, vol. 13, no. 2, pp. 347–353, 1998.

[26] A. Abur and J. Zhu, “Identification of parameter errors,” in *Power and Energy Society General Meeting, 2010 IEEE*, 2010, pp. 1–4.

[27] C. N. Lu, J. H. Teng, and W.-H. E. Liu, “Distribution System State Estimation,” *IEEE Trans. Power Syst.*, vol. 10, no. 1, pp. 229–240, 1995.

[28] M. Baran and T. McDermott, “Distribution system state estimation using AMI data,” in *Power Systems Conference and Exposition*, 2009, vol. 15236, pp. 1–3.

[29] M. E. Baran and A. W. Kelley, “A Branch-Current-Based State Estimation Method for Distribution Systems,” *IEEE Trans. Power Syst.*, vol. 10, no. 1, pp. 483–491, 1995.

[30] H. Wang and N. N. Schulz, “A Revised Branch Current-Based Distribution System State Estimation Algorithm and Meter Placement Impact,” *IEEE Trans. Power Syst.*, vol. 19, no. 1, pp. 207–213, 2004.

[31] M. Baran, J. Jung, and T. McDermott, “Including voltage measurements in branch current state estimation for distribution systems,” in *Power and Energy Society General Meeting*, 2009, no. 1, pp. 1–5.

[32] C. Gómez-Quiles, “State Estimation for Smart Distribution Substations,” *IEEE Trans. Smart Grid*, vol. 3, no. 2, pp. 986–995, 2012.

[33] “Vision of the Future Grid.”

[34] P. Zarco and A. Gomez-Exposito, “Power system parameter estimation: a survey,” *IEEE Trans. Power Syst.*, vol. 15, no. 1, pp. 216–222, 2000.

[35] A. S. Debs, “Estimation of Steady-State Power System Model Parameters,” *IEEE Trans. Power Appar. Syst.*, vol. PAS-93, no. 5, pp. 1260–1268, 1974.

[36] I. W. Slutsker, S. Mokhtari, and K. A. Clements, “Real Time Recursive Parameter Estimation in Energy Management Systems,” *IEEE Trans. Power Syst.*, vol. 11, no. 3, pp. 1393–1399, 1996.

[37] J. Liu, J. Tang, F. Ponci, A. Monti, C. Muscas, and P. A. Pegoraro, “Trade-Offs in PMU Deployment for State Estimation in Active Distribution Grids,” *IEEE Trans. Smart Grid*, vol. 3, no. 2, pp. 915–924, 2012.

[38] W.-H. E. Liu and S.-L. Lim, “Parameter Error Identification and Estimation in Power System State Estimation,” *IEEE Trans. Power Syst.*, vol. 10, no. 1, pp. 200–209, 1995.

[39] S. A. Arafeh and R. Schinzinger, “Estimation Algorithms for Large-Scale Power Systems,” *IEEE Transactions on Power Apparatus and Systems*, vol. PAS-98, no. 6. pp. 1968–1977, 1979.

[40] Y. Zhang and M. Larsson, “Static Error Identification: Application to Line Parameter Estimation,” *2010 Int. Conf. Power Syst. Technol.*, pp. 1–6, Oct. 2010.

[41] V. Quintana and T. Van Cutsem, “Real-Time Processing of Transformer Tap Positions,” *Can. Electr. Eng. J.*, vol. 12, no. 4, pp. 171–180, 1987.

[42] V. Quintana and T. Van Cutsem, “Power System Network Parameter Estimation,” *Optim. Control Appl. Methods*, vol. 9, pp. 303–323, 1988.

[43] W.-H. E. Liu, F. F. Wu, and S.-M. Lun, “Estimation of Parameter Errors from Measurement Residuals in State Estimation,” *IEEE Trans. Power Syst.*, vol. 7, no. 1, pp. 81–89, 1992.

[44] M. B. Do Coutto Filho, J. C. Stacchini de Souza, and E. B. M. Meza, “Off-line Validation of Power Network Branch Parameters,” *Gener. Transm. Distrib. IET*, vol. 2, no. 6, pp. 892–905, 2008.

[45] L. Zhang and A. Abur, “Identifying Parameter Errors via Multiple Measurement Scans,” *IEEE Trans. Power Syst.*, vol. 28, no. 4, pp. 3916–3923, 2013.

[46] M. R. M. Castillo, J. B. A. London, N. G. Bretas, S. Lefebvre, J. Prevost, and B. Lambert, “Offline Detection, Identification, and Correction of Branch Parameter Errors Based on Several Measurement Snapshots,” *IEEE Trans. Power Syst.*, vol. 26, no. 2, pp. 870–877, 2011.

[47] K. F. Riley, M. P. Hobson, and S. J. Bence, *Mathematical Methods for Physics and Engineering*, Second edi. Cambridge: University Press, 2002.

[48] A. Abur, *Power System State Estimation Theory and Implementation*. Marcel Dekker, Inc.

[49] A. Gomez-Exposito, C. Gomez-Quiles, and I. Dzafic, “State Estimation in Two Time Scales for Smart Distribution Systems,” *IEEE Transactions on Smart Grid*, vol. 6, no. 1. pp. 421–430, 2015.

[50] W. Kersting, *Distribution System Modeling and Analysis - Third Edition*. CRC Press, 2012.

[51] K. Samarakoon, J. Wu, J. Ekanayake, and N. Jenkins, “Use of delayed smart meter measurements for distribution state estimation,” *Power and Energy Society General Meeting, 2011 IEEE*. pp. 1–6, 2011.

[52] A. Cataliotti, P. Russotto, D. Di Cara, E. Telaretti, and G. Tine, “New measurement procedure for load flow evaluation in medium voltage smart grids,” *Instrumentation and Measurement Technology Conference (I2MTC), 2013 IEEE International*. pp. 517–522, 2013.

[53] D. Ablakovic, I. Dzafic, R. A. Jabr, and B. C. Pal, “Experience in distribution state estimation preparation and operation in complex radial distribution networks,” *PES General Meeting | Conference & Exposition, 2014 IEEE*. pp. 1–5, 2014.

[54] L. Holten, A. Gjelsvik, S. Aam, F. F. Wu, and W.-H. E. Liu, “Comparison of different methods for state estimation,” *IEEE Trans. Power Syst.*, vol. 3, no. 4, pp. 1798–1806, 1988.

[55] C. W. Hansen and A. S. Debs, “Power System State Estimation Using Three-Phase Models,” *IEEE Trans. Power Syst.*, vol. 10, no. 2, pp. 818–824, 1995.

[56] W. Kersting, “Radial Distribution Test Feeders,” *IEEE/PES Eng. Soc. Winter Meet.*, 2001.

[57] D. P. Chassin, K. Schneider, and C. Gerkensmeyer, “GridLAB-D: An Open-source Power Systems Modeling and Simulation Environment,” *Transmission and Distribution Conference and Exposition*. pp. 1–5, 2008.

[58] R. F. Arritt and R. C. Dugan, “The IEEE 8500-node test feeder,” *Transmission and Distribution Conference and Exposition, 2010 IEEE PES*. pp. 1–6, 2010.

[59] A. Gómez-Expósito, A. Abur, A. de la Villa Jaén, and C. Gómez-Quiles, “A Multilevel State Estimation Paradigm for Smart Grids,” *Proc. IEEE*, vol. 99, no. 6, 2011.

Distribution

No. of Copies	
1	Dan Ton Department of Energy, 1000 Independence Ave SW Mailstop OE-10 Washington, DC 20585
1	Chen-Ching Liu Washington State University P O Box 647275 Pullman, WA 99164-2752

No. of Copies		
3	**Local Distribution**	
	Pacific Northwest National Laboratory	
	Kevin Schneider	(PDF)
	Frank Tuffner	(PDF)
	Tess Williams	(PDF)

Pacific Northwest
NATIONAL LABORATORY

U.S. DEPARTMENT OF
ENERGY

Proudly Operated by **Battelle** *Since 1965*

902 Battelle Boulevard
P.O. Box 999
Richland, WA 99352
1-888-375-PNNL (7665)

www.pnnl.gov